Large Eddy Simulation of Atomizing Sprays

Grosshans, Holger

2013

Large Eddy Simulation of Atomizing Sprays

Doctoral Thesis

Holger Großhans

Division of Fluid Mechanics
Department of Energy Sciences

Lund, Sweden, 2013

LUNDS UNIVERSITET

ISBN 978-91-7473-463-8
ISSN 0282-1990
ISRN LUTMDN/TMHP-13/1090 - SE

Division of Fluid Mechanics
Department of Energy Sciences
Faculty of Engineering
Lund University
Box 118
S-221 00 LUND
Sweden

Typeset in LaTeX
Printed by Media-Tryck, Lund, March 2013.

Populärvetenskaplig Sammanfattning

Vätska-gas tvåfasströmning förekommer ofta i det vardagliga livet, i naturen, exempelvis fallande regndroppar eller vågor i havet, samt industriella applikationer, t.ex. bränsleinjektion i dieselmotorer eller gasturbiner. För många av dessa tillämpningar är samspelet mellan vätska och gas avgörande för en effektiv drift. I detta arbete studeras vätska-gas interaktion numeriskt, speciellt för atomiserande flöden. Large Eddy Simulations (LES) utförs för att erhålla tidsberoende resultat. vätskestråle uppbrott och bildandet av små sfäriska droppar simuleras med hjälp av Volume of Fluid (VOF) metoden. Utvecklingen av vätskesprejer är upplösningen i mindre droppar, evaporation och blandningen med den omgivande gasen simuleras med hjälp av Lagrangian Particle Tracking (LPT) metoden. Denna avhandling fokuserar på a) att förbättra förståelsen av den underliggande fysiken och b) att förbättra de numeriska modelleringstekniker för atomiserande tvåfasströmningar. Beträffande fysiken av tvåfasströmningar, så studeras hur variationer av vätskans egenskaper, som densitet, viskositet eller ytspänning påverkar den primära uppbrytning av vätskestrålen, sprej utveckling och vätska-gas blandning. Där visas hur viskositet och ytspänning stabiliserar vätske strukturer, medan högre vätskedensitet leder till snabbare likvid brytning. Även pulserande injektion och dess effekt på primär uppbrott och sprejutveckling studeras. Indragning är indikerad vilken utbreder sig snabbare än själva strålen och ökar vätska-gas blandning. Beträffande numerisk modellering av tvåfasströmningar, så utvecklats en ny metod för att koppla en VOF simulering av strålens uppbrytning med en LPT simulering av en finfördelad sprej. Metoden bygger på en statistisk koppling som visar sig vara korrekt och förbättra betydligt beräkningseffektivitet jämfört med de existerande VOF-LPT kopplingsmetoderna. En ny metod föreslås för att korrelera sprej resultat som erhållits från mätningar till numeriskt erhållna sprej data. Istället för att enbart jämföra globala sprej parametrar, jämförs det kompletta fältet av en variabel, dvs. ljusets extinktionskoefficient.

Abstract

Liquid-gas two-phase flows occur frequently in daily life, in nature e.g. falling rain drops or waves in the sea, and in industrial applications, e.g. fuel injection in Diesel engines or gas turbines. For many of these applications the interaction between liquid and gas is crucial for their efficient operation. In this work liquid-gas interaction is studied numerically, specifically for atomizing flows. Large Eddy Simulations (LES) are performed to obtain time-dependent results. The disintegration of a liquid jet and the formation of small spherical droplets is simulated using the Volume of Fluid (VOF) method. The development of liquid sprays, the breakup into smaller droplets, the evaporation and mixing with the surrounding gas is simulated using the Lagrangian Particle Tracking (LPT) method. This thesis focuses a) on improving the understanding of the underlying physics and b) improving the numerical modelling techniques of atomizing two-phase flows.

Concerning physics of two-phase flows, it is studied how variations of the liquid properties, such as density, viscosity or surface tension influence the primary breakup of the liquid jet, the spray development and the liquid-gas mixing. It is shown how viscosity and surface tension stabilise the liquid structures, while higher liquid density leads to faster liquid breakup. Also pulsed injection and its effect on primary breakup and the spray development is studied. The formation of an entrainment wave is indicated which propagates faster than the jet itself and enhances liquid-gas mixing.

Concerning numerical modelling of two-phase flows, a novel method is developed to couple a VOF simulation of the jet atomization with a LPT simulation of a dispersed spray. The method is based on a statistical coupling which shows to be accurate and to improve significantly the computational efficiency compared to existing VOF-LPT coupling methods. Also, a novel approach to correlate spray data obtained from measurements to numerically obtained spray data is proposed. Instead of only global spray parameters, a complete field of a variable, the light extinction coefficient, is compared.

CONTENTS

NOMENCLATURE

Roman symbols

a	number of SLIPI images (-)
A	area (m^2)
b	damping constant (kg/s)
c_p	specific heat capacity at constant pressure ($J/(kg \cdot K)$)
d	diameter (m)
D_m	molecular mass diffusivity (m^2/s)
D_{th}	molecular thermal diffusivity (m^2/s)
E	energy (J)
f	statistical number of droplets per unit volume ($1/m^3$)
F	force (N)
g	gravitational constant (m/s^2)
G	filter function (-)
h	cell size (m)
h_L	latent heat (J/kg)
h_m	convective mass transfer coefficient ($J/(s \cdot m^2 \cdot K)$
h_{th}	convective heat transfer coefficient ($J/(s \cdot m^2 \cdot K)$
I	light intensity (W/m^2)
k	turbulent kinetic energy (m^2/s^2)
l	length (m)
L	characteristic length scale (m)

m	mass (kg)
N	number density ($1/m^3$)
n_i	interface unit normal (-)
p	pressure (N/m^2)
Q	heat flux ($J/(m^2 \cdot s)$)
r	position (m)
R	specific gas constant ($J/(kg \cdot K)$)
s	autocorrelation function (-)
S	SLIPI image intensity (W/m^2)
t	time (s)
T	temperature (K)
U	characteristic velocity scale (m/s)
u_i	flow velocity in i-direction (m/s)
V	volume (m^3)
y	distortion parameter (-)
Y	mass fraction (-)
Z	mixture fraction (-)

Greek symbols

α	liquid phase volume fraction (-)
β	WENO smoothness indicators (-)
γ	WENO linear weights (-)
δ	Dirac function (-)
ε	dissipation rate of turbulent kinetic energy ($J/(kg \cdot s)$)
ϵ	very small number (-)
ζ	thermal conductivity ($J/(s \cdot m \cdot K)$)
θ	gas phase volume fraction (-)
κ	interface curvature (-)
λ	wavelength (m)
μ	dynamic viscosity ($kg/(m \cdot s)$)
μ_e	extinction coefficient ($1/m$)
ν	kinematic viscosity (m^2/s)
ϖ	solid angle (°)
ρ	density (kg/m^3)
ϱ	refractive index (-)
σ	surface tension (N/m)

σ_e	extinction cross-section (m^2)
ς	spring constant (kg/s^2)
τ	timescale (s)
τ_{ij}	viscous stress (N/m^2)
ϕ	arbitrary variable
φ	angle (°)
χ	apparent order of the numerical method (-)
ψ	numerical uncertainty (-)
ω	WENO weighting factor (-)
Θ	wave number (1/m)
Λ	distance function (m)

Subscripts

0	integral scale
d	droplet
f	flow
fax	Faxen
g	gas
in	inertial
inj	injection
jet	jet
l	liquid
noz	nozzle
p	parcel
r	radiative
rel	relative
s	surface
spa	spanwise
str	streamwise
S	source
T	turbulence
vm	virtual mass
w	drag
x,y,z	spatial coordinates (m)
η	Kolmogorov scale (m)
λ	Taylor scale

Abbreviations

CFD	Computational Fluid Dynamics
CL	Coupling Layer
DCA	Direct Coupling Approach
DNS	Direct Numerical Simulation
FDM	Finite Difference Method
FVM	Finite Volume Method
LES	Large Eddy Simulation
LPT	Lagrangian Particle Tracking
pdf	probability density function
RANS	Reynolds Averaged Navier-Stokes
SCA	Statistical Coupling Approach
SGS	Sub Grid Scale
SLIPI	Structured Laser Illumination Planar Imaging
SMD	Sauter Mean Diameter
VOF	Volume of Fluid

Non-dimensional numbers

Nu	Nusselt number	$Nu = \frac{h_{th} L}{\zeta}$
Oh	Ohnesorge number	$Oh = \frac{\mu}{\sqrt{\rho \sigma L}}$
Pr	Prandtl number	$Pr = \frac{\nu}{D_{th}}$
Re	Reynolds number	$Re = \frac{UL}{\nu}$
Sc	Schmidt number	$Sc = \frac{\nu}{D_m}$
Sh	Sherwood number	$Sh = \frac{h_m L}{D_m}$
St	Stokes number	$St = \frac{\tau_d}{\tau_f}$
We	Weber number	$We = \frac{\rho U^2 L}{\sigma}$

CHAPTER 1

INTRODUCTION

1.1 Context and Motivation

There are four states matter can take on in our observable environment. Most matter in the universe exists in plasma state, while the gaseous, liquid and solid states occur most frequently in everyday life, see Fig. 1.1, and are therefore considered here. Even if formally not completely correct, the term phase is often used as a synonym for state of matter. If a flow consists of at least two phases, it is called a multiphase flow. Multiphase flows occur frequently in nature, for example when an iceberg is dragged by the wind through the sea or when ocean waves hit the shore. The waves are created by the interaction between the water surface and the wind, while the water interacts at the same time with the sand at the sea ground. If only two phases participate the flow is called a two-phase flow. Natural two-phase flows are e.g. falling rain drops, sand storms in the desert or the eruptions of geysers. Two-phase flows are frequent in industrial applications, e.g. aerosol sprays, fuel injection in Diesel engines, steam generators in nuclear reactors, stationary gas turbines to produce electrical or aircraft mounted jet engines to provide mechanical power.

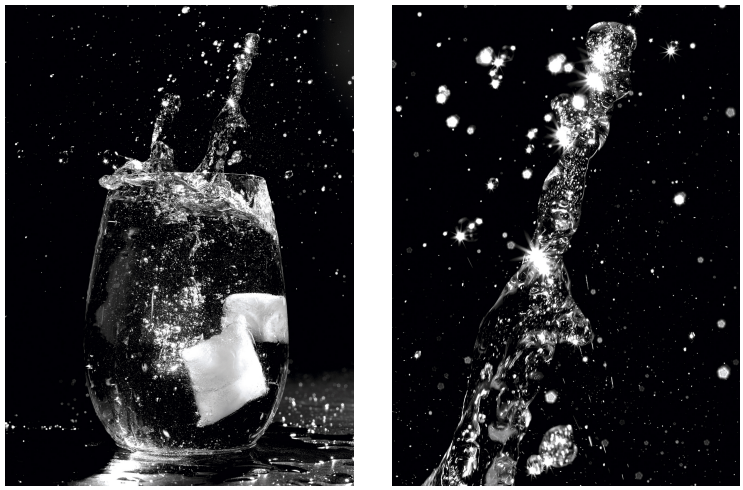

Figure 1.1: A typical multiphase flow (by anysmith.com).

Fuel Injection

For many of these industrial applications the interaction between liquid and gas is crucial for their efficient operation. For example, in aircraft mounted jet engines, only liquid fuels are used, due to their high specific energy. The drawback of liquid fuels is that it is much more difficult to obtain sufficient air-fuel mixing as compared to gaseous fuels. The liquid fuel is injected into an airstream; due to instabilities the fuel jet breaks up into irregular liquid structures, which will further break up into a spray of small droplets and will finally evaporate. This air-fuel mixing process is of high influence on the following combustion and is, thus, of high importance for the power of the engine and its level of emissions. The most dominant mechanisms, which cause the fuel jet to break up, are cavitation in the fuel injection nozzle, turbulence in the fuel jet and aerodynamic interaction between the jet and the surrounding turbulent gas flow [1]. In gas turbines, the last mechanism is realised by creating a high relative velocity between the fuel stream and the gas. For aircraft jet engines, two methods can be distinguished: the fuel jet is injected with a high velocity in slow moving gas, this is called *pressure atomization*. The other possibility is to inject the fuel jet with a slow velocity in fast

moving gas, this is called *airblast atomization* [2].

The atomization of a fuel with a pressure atomizer is realised by pressing the fuel with a high pressure through a small orifice. If the orifice would be a simple drill hole, the spreading of the resulting spray would not be wide enough. A wider spreading is reached by giving the fuel jet a spinning motion. Therefore, the so-called simplex nozzle was developed: here the spin is realised by tangential holes inside the nozzle, which give the fuel a rotational motion at the orifice. This results in a very good atomization for high fuel volume flows. But as the atomization capability is significantly reduced for lower fuel flows, which are used at cruise flight in high altitude, simplex nozzles are not used for aircraft jet engines anymore [3]. This led to the development of the duplex nozzle, which is a pressure atomizer with two orifices. The small, inner one is opened for low liquid mass flows and the larger outer one opens for higher liquid mass flows. Through this, a sufficient atomization is maintained for a broad range of mass flows, without requiring an overly high injection pressure.

In an airblast atomizer, the low speed fuel jet is usually first spread into a sheet and then exposed to a swirling gas flow, where the swirling motion enhances instabilities and increases the breakup. The gas flow can be either of high velocity and low mass flow, which is called air-assisted atomizing, or of low velocity and large mass flow, which is actually called airblast atomizing. Besides pressure atomization and airblast atomization, in rare cases vaporisers have been applied in aircraft jet engines: The fuel and gas are transported through a pipe which is located in the combustion chamber in the region of the flame. The fuel vaporises and is injected into the combustion chamber in gaseous state.

A method that has shown to improve air-fuel mixing in internal combustion engines is the pulsed fuel injection. While its original purpose was to create stratified cylinder loadings, enhanced mixing due to increased air entrainment was observed. On the other hand, too fast mixing can also lead to undesired lean mixtures.

In general, it can be stated that one wishes to understand the mechanisms of liquid-gas instabilities, of breakup and mixing in order to be able to control them.

Experimental Works

A large number of experiments has been carried out, e.g. [4–7], applying various imaging techniques, but multiple scattering effects are introduced when illuminating the optically dense region. Hence, most of these techniques are limited to the identification of droplets in dilute regions or more global parameters characterising the spray. Modern experimental techniques such as SLIPI [8] can reduce this noise arising from multiply scattered photons and resolve droplets of a minimum diameter of about 20 μm [9]. However, the limitations of the today available experimental techniques are the reason why experiments are not sufficient to provide enough details for full understanding of the mechanisms involved in atomizing two-phase flows. To obtain a higher spatial- and temporal resolution numerical simulations are the most appropriate alternative.

Numerical Works

The numerical modelling of two-phase flows is challenging compared to single-phase flows: a wide range of length- and timescales are involved, depending on the flow regime different mechanisms need to be captured and the phase interface leads to high gradients in the flow field. The case of an atomizing two-phase flow can be divided into three stages: a) the flow inside the nozzle, b) the liquid jet exiting the nozzle and its disintegration and c) the liquid spray, its breakup into smaller droplets and its evaporation. Different numerical methods are required in each stage, as different physical mechanisms are dominant and the involved length- and timescales differ widely. In the early works [10, 11] the governing equations for two-phase flows were derived and applied in the fluid-fluid formulation. Both phases are averaged over a fixed volume. Each phase is individually described in Eulerian framework and closure terms are applied to model the liquid-gas interaction. The averaging volume is large compared to the droplet size, thus, no information on the individual droplet level is available. However, due to its low computational effect this approach still shows good capabilities of simulating large scale flows, e.g. in [12]. When the available computer power increased, new modelling techniques, such as Lagrangian modelling of the dispersed phase and approaches that resolve the gas-liquid interface, were developed.

If in-nozzle flows are simulated for the purpose of studying the spray development, the two main phenomena that are of interest are cavitation and in-nozzle turbulence. Due to the concave nozzle shape, the pressure in the liquid flow decreases and cavitation bubbles are formed. These bubbles implode when leaving the nozzle and enhance the breakup of the liquid jet. Turbulent structures that are formed inside the nozzle and leaving it through the orifice, have the same effect. In-nozzle flows are usually described in Eulerian framework and the vapour is either tracked in Lagrangian manner or by an interface resolving approach. Phase changes are accounted for by a cavitation model, e.g. the Rayleigh-Plesset equation. Numerical works show the great influence of cavitation on the resulting breakup properties of the liquid jet [13–15].

To simulate the liquid jet and the dense spray region, interface resolving approaches such as the Volume of Fluid (VOF) or the level-set method are often applied. These methods are natural for cases with immiscible fluids and reflect the physics to a high degree. However, high spatial resolution is required in order to capture the time dependent shape variations of the liquid structures. This, in turn, implies that the approach is computationally too expensive to be applied for two-phase flows with high interface curvature, e.g. in a dilute spray region with small droplets. The VOF approach has been chosen in this work in order to be able to handle the primary breakup of the liquid jet and the dense spray region, due to the fact that it contains irregular liquid structures. In the past, Reynolds Averaged Navier-Stokes (RANS) simulations using the VOF method have been performed, e.g. in [16]. However, the liquid structures can only be resolved with the RANS approach, if the droplet and turbulent scales are separated. This is usually not the case for spray applications. Recently, Direct Numerical Simulation (DNS) has been applied [17, 18] to analyse time dependent two-phase phenomena. DNS is computationally expensive, limited to relatively low Reynolds numbers and leads in the mentioned cases to 134 million, respectively 400 million grid points. To capture unsteady mechanisms and to limit computational costs, in this work Large Eddy Simulations (LES) are performed. Thereby, it is possible to handle larger Reynolds numbers, but limits the size of droplets that can be resolved.

For more than 40 years the Lagrangian Particle Tracking (LPT)

method is applied to simulate sprays [19]. As this method is computationally fast, it has been used extensively to study sprays. The macroscopic structure of the spray, i.e. spray penetration and the Sauter Mean Diameter (SMD) of the droplets depending on the axial and radial distance from the nozzle has been studied, for example in [20]. The effect of different fuel types has been studied [21], the effect of the droplet size distribution on mixing has been analysed [22] and the effect of the droplet Stokes numbers on the spray shape has been investigated in [23]. However, due to the underlying assumptions, the LPT approach is only valid for the dilute spray regions.

The final aim of two-phase flow simulations, is to be able to describe the flow numerically accurate and consistent throughout all stages. Therefore, there have been several attempts to couple numerical methods with each other. E.g. in [24] the VOF method has been coupled to the LPT method. The breakup of the liquid jet is simulated with a VOF method. When a droplet reaches a state where the assumptions of the LPT method are valid, it will be extracted from the VOF simulation and introduced in the LPT simulation. In [25] even the in-nozzle flow was simulated, but cavitation was not included. Starting from the velocity distributions at the nozzle exit plane, the Refined Level Set Grid method (an interface capturing method like VOF) was applied to simulate the jet breakup. The resulting droplets were coupled to a LPT simulation. As in [24], the droplets were transferred individually to LPT. This is respecting the physical assumptions in the whole computational domain and it is much faster than a pure VOF simulation. However, this coupling approach is still computationally too expensive to simulate a complete spray until evaporation. The coupling of numerical methods is not straight forward and there has not yet been found a method to describe a spray accurately and consistently from the in-nozzle flow to evaporation.

1.2 Research Objectives

The numerical modelling techniques of atomizing two-phase flows are today incomplete. Due to limited computational resources, one needs to take assumptions, introduce simplifications, and neglect certain phys-

ical effects or compromise in terms of the computational domain size. Thus, and due to the fact that also experimental observation techniques are limited, the physics of such flows is still not completely understood. Therefore this thesis focuses on the **advancement of the numerical modelling** and the **improvement of the understanding of the underlying physics** of two-phase flows. Concretely, the following questions are answered :

- What is the effect of variations in the liquid properties, such as density, viscosity or surface tension, on the break up behaviour of a jet?
- What is the effect of variations in the liquid properties, such as density, viscosity or surface tension, on the development of a spray and the mixing of the liquid with the surrounding gas?
- What is the effect of pulsed liquid injection on the liquid-gas mixing?
- How can the primary break-up of a liquid jet and the subsequent break up of droplets and evaporation be modelled consistently, despite their vast difference in time and length scales?
- How can numerical and experimental data be correlated to validate the spray modelling?

1.3 Contributions

As main contributions of this thesis, answers to the above raised questions are provided. These are summarised in the following.

Sensitivity Analysis of the Spray Development depending on varying Liquid Properties

Sensitivity studies have been performed to study the effect of variations in liquid properties like density, surface tension or viscosity on the flow. The influence on the primary breakup has been studied by applying the

VOF method, the influence on the dilute spray has been studied by applying the LPT method. For the investigated range of the properties, the analysis has shown the stabilising effect of viscosity and surface tension and the destabilising effect of increased liquid and gas density.

Pulsed Injection

It has been shown that the tail of an injection pulse propagates faster than its head. This indicates the formation of an entrainment wave that propagates faster than the jet itself and leads to enhanced mixing liquid-gas mixing.

Statistical VOF-LPT Coupling

A novel approach has been developed to couple a VOF simulation of the primary break-up of a liquid jet to a LPT simulation of a spray. The approach is based on the idea that statistical distributions of droplets, created by the jet break up are transferred to the LPT simulations, instead of transferring each droplet individually. This approach shows an accurate modelling and a significant improvement in computational efficiency.

Correlation of Numerical and Experimental Spray data

A novel approach has been developed to correlate numerical and experimental spray data. While earlier works compare only global parameters of the spray, such as spray penetration length or spray opening angle, here a complete field of a variable is compared, the light extinction coefficient. It can be extracted experimentally by applying the Dual-SLIPI technique, which suppresses multiple scattered light, and it is derived numerically from the results of the LPT simulations.

CHAPTER 2

PHYSICAL FOUNDATIONS OF FLUID FLOWS

2.1 Laminar and Turbulent Single Phase Flows

2.1.1 Laminar or Turbulent Flow

Osborne Reynolds conducted in 1883 a classical experiment when he put a dye in the centre of a pipe flow to visualise a streakline. For low flow-rates the streakline shows to be straight and undisturbed, only blurred due to molecular diffusion. This is denoted as *laminar flow*. When the flow-rate is increased, the streakline starts to fluctuate and shows an irregular behaviour. This is denoted as *transitional flow*. When increasing the flow-rate further the flow shows to be random, dissipative, diffusive, irregular and three dimensional. The flow exhibits a wide range of length- and timescales. This is denoted as *turbulent flow*. As Reynolds showed, the transition point between the flow characteristics depends on a dimensionless number, consequently called Reynolds number. It relates inertia to the effects of viscosity and is defined as

$$Re \;=\; \frac{UL}{\nu}\;. \tag{2.1}$$

Up to a certain value the viscous forces damp the small scale disturbances in the flow. Above that value the flow will become unstable and change

from laminar to turbulent.

2.1.2 Energy Cascade and Kolmogorov Hypotheses

In 1922, Richardson developed the idea of the *turbulence energy cascade*: turbulence is composed of eddies of various characteristic length-, velocity- and timescales, l, $u(l)$ and $\tau(l)$. Turbulent kinetic energy is produced on the large scales of motion, l_0. At these large scales the effects of viscosity are small compared to inertial effects and, thus, the Reynolds number of these eddies is large. At large Reynolds numbers, the larger eddies are unstable and break up into smaller eddies by processes which are again not affected by viscosity. The smaller eddies in turn break up into even smaller ones until their size is sufficiently small whereby viscosity becomes important and the eddy Reynolds number becomes small. Due to the small scale of these eddies, viscous dissipation becomes important; this inhibits the accumulation of turbulent structures of small sizes. The concepts described here, of energy being converted (i.e. transferred) from larger eddies to small ones, is called often as the energy cascade. In general, turbulent energy is transferred from the large to the small scales, but locally and intermittently energy can also be transferred from the small to the large scales; this is referred to as backscatter. As [26] showed, this effect can be significant; the backscattered energy can locally be even larger then the net transferred energy. The energy content E of a fully turbulent flow as a function of the wave number Θ is schematically shown in Fig. 2.1.

Kolmogorov quantified the energy cascade in 1941. While the large scale eddies are highly affected by the dimensions of the domain and, therefore, are often anisotropic, Kolmogorov argued that the directional information will get lost when eddies break up on their way down the energy cascade. As a conclusion, he stated a hypothesis for the small scale eddies [27]:

Kolmogorov's first hypothesis of local isotropy: at sufficiently high Reynolds numbers, the small-scale turbulent motions ($l \ll l_0$) are statistically isotropic.

A length scale l_{EI} can be defined, which distinguishes between a range of anisotropic and a range of isotropic eddies. As the eddies that

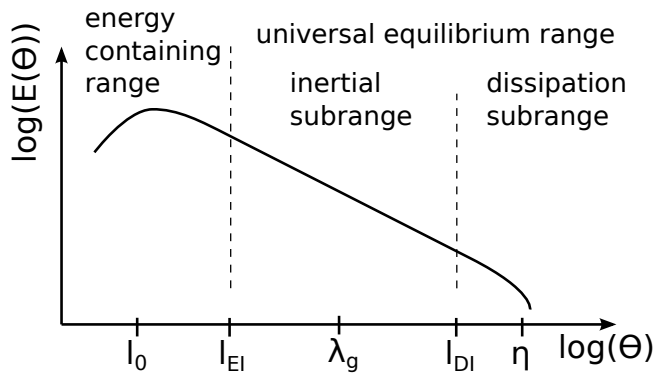

Figure 2.1: Energy spectrum of a turbulent flow as a function of the wave number Θ.

are larger than this scale contain the most kinetic energy, their range of scales is called the *energy containing range*. For the isotropic eddies Kolmogorov claimed that their statistics are universal and only depending on the two most influencing parameters, viscosity and the dissipation rate of the turbulent kinetic energy, ε. Thus he stated:

Kolmogorov's second similarity hypothesis: in every turbulent flow at sufficiently high Reynolds numbers, the statistics of the small-scale motions ($l < l_{EI}$) have a universal form that is uniquely determined by ν and ε.

This range of scales is called the *universal equilibrium range*. As only eddies of the smallest scales (l_η) are affected by viscosity, eddies in a range between l_0 and l_η depend only on the dissipation rate. Therefore Kolmogorov stated:

Kolmogorov's third similarity hypothesis: in every turbulent flow at sufficiently high Reynolds numbers, the statistics of the motions of scale l in the range $l_0 \gg l \gg l_\eta$ have a universal form that is uniquely determined by ε and independent of ν.

A length scale l_{DI} can be defined, which distinguishes between the ranges of scales of those eddies which motions are affected by inertia and those that are affected by inertia and dissipation. This length scale divides the universal equilibrium range in the *inertial subrange* and the *dissipation range*.

2.1.3 Scales of Turbulence

Based on the Kolmogorov hypotheses and dimensional analysis, some useful length-, velocity- and timescales of turbulent motion can be defined.

Integral Scales

A characteristic eddy in the energy containing range is of the order of the *integral length scale*. Considering homogeneous isotropic turbulence with zero mean velocity, it can be derived based on the autocorrelation function of the fluctuating velocity, given by

$$s(r) = \frac{\langle u(x)u(x+r)\rangle}{\langle u(x)u(x)\rangle} \ . \tag{2.2}$$

Here, $\langle\phi\rangle$ denotes the time average of a quantity and u the velocity fluctuation. The integral length scale, l_0, represents a measure of the distance at which velocity fluctuations are correlated and is defined as

$$l_0 = \int_0^\infty s(r)dr \ . \tag{2.3}$$

A corresponding time scale can be defined as

$$\tau_0 = \frac{l_0}{u_0} \ , \tag{2.4}$$

where the velocity scale is of the order of the root mean square of the velocity fluctuations. For the large scales the turbulence Reynolds number, Re_T, is given by

$$Re_T = \frac{u_0 l_0}{\nu}. \tag{2.5}$$

Taylor Scales

A length scale can be derived from the second derivative at the origin of the autocorrelation function as

$$l_\lambda = \frac{1}{\sqrt{-0.5 \cdot \frac{d^2 s(r)}{dr^2}|_{r=0}}} \,. \tag{2.6}$$

Eddies of this scale are called *Taylor scale eddies* and show to be located in the inertial subrange. Their size is between the largest and the smallest eddies. Their relation to the integral length scale was derived in [28] as

$$l_\lambda / l_0 \sim Re_T^{-1/2} \,. \tag{2.7}$$

Kolmogorov Scales

The smallest eddies in the flow, called *Kolmogorov scale eddies* have the length-, velocity- and timescale l_η, u_η and τ_η, respectively. By using dimensional analysis and Kolmogorov's hypothesis one finds that they are of the order

$$l_\eta = \left(\frac{\nu^3}{\varepsilon}\right)^{1/4}, \qquad u_\eta = (\nu\varepsilon)^{1/4} \qquad \text{and} \qquad \tau_\eta = \left(\frac{\nu}{\varepsilon}\right)^{1/2}. \tag{2.8}$$

The scales of the integral and the Kolmogorov eddies are related by

$$l_\eta / l_0 \sim Re_T^{-3/4}, \qquad u_\eta / u_0 \sim Re_T^{-1/4} \qquad \text{and} \qquad \tau_\eta / \tau_0 \sim Re_T^{-1/2}. \tag{2.9}$$

2.2 Multiphase Flow Types and Definitions

2.2.1 Multiphase Flow Types

If plasma is not considered, the solid, liquid and gaseous phase exist in our observable environment, if plasma is not considered. A fluid flow that consists of at least two of these phases is called a multiphase flow. Thus, the type of the flow is either a

- solid-liquid-gas flow,

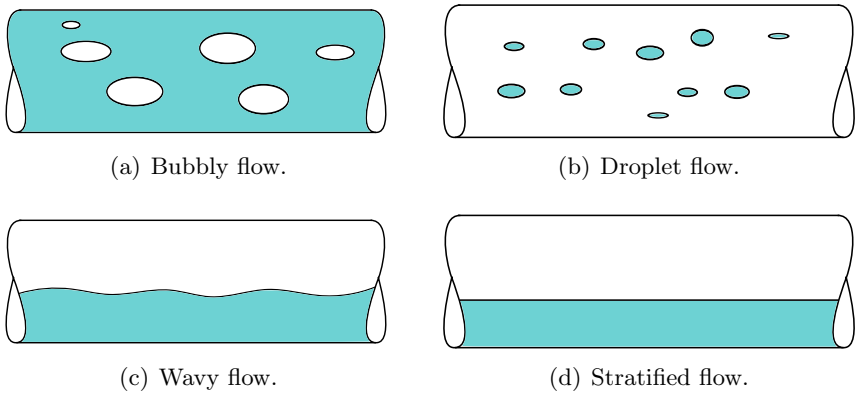

(a) Bubbly flow. (b) Droplet flow.

(c) Wavy flow. (d) Stratified flow.

Figure 2.2: Two-phase flow regimes. The blue surface denotes liquid, the white surface gaseous phase.

or, if only two phases are involved

- a solid-liquid flow,
- a solid-gas flow or
- a liquid-gas flow.

In this work two-phase flows are studied involving a liquid and a gaseous phase. There are numerous flow regimes defined for gas-liquid flows, depending on the fluid properties, the gas flow rate and the liquid flow rate. For example, a flow where the liquid phase is continuous and the gaseous phase occurs in small bubbles is called a bubbly flow (Fig. 2.2(a)). If the gaseous phase is continuous and the liquid phase appears in dispersed droplets it is called a droplet flow (Fig. 2.2(b)). A flow where the liquid and the gaseous flow are both continuous is called a wavy flow (Fig. 2.2(d)) or a stratified flow (Fig. 2.2(b)). Here, the flow regimes are studied that occur when a liquid is injected with a high pressure into a gaseous environment, which is called an *atomizing jet* (Fig. 2.3). The term atomizing originates from the fact that the liquid breaks up fast into very small, i.e. atomized, structures.

2.2.2 Instability Mechanisms

Instability implies that a given disturbance grows. Instability of a droplet implies that disturbances grow and lead to droplet deformation which ultimately leads to breakup of the liquid structure. The break-up mechanism is not unique and different processes have been identified, leading to droplets of different sizes. Two types of liquid breakup are generally distinguished: the breakup of the liquid jet, which is referred to as primary breakup (Ch. 2.3.3), and the further breakup of the structures produced during primary breakup into smaller droplets, which is referred to as secondary breakup (Ch. 2.3.4). For both types, different breakup regimes can be identified, which lead to different results for e.g. breakup length of the liquid jet or resulting droplet diameters. The different breakup regimes are caused by instability mechanisms, which are in principle the same for primary and secondary breakup. The Rayleigh-Taylor instability is named after Lord Rayleigh and Geoffrey Ingram Taylor, who first investigated the phenomenon [29,30]. It occurs at the interface of two fluids of different densities, when the two fluids move relative to each other. The formation of mushroom cap shapes in the lighter fluid is typical. The Kelvin-Helmholtz instability is named after Lord Kelvin and Hermann von Helmholtz, who investigated the phenomenon in [31] and [32]. It occurs due to shear forces at the interface, when two fluids move with different velocities to each other. Another instability mechanism, which is only applicable to primary breakup, is caused by cavitation in the injection nozzle. This is due to vapour bubbles that form in the liquid due to rapid pressure changes in the nozzle flow. When these bubbles implode the may lead to the breakup of the jet into a large number of very small droplets.

2.2.3 Dimensionless Numbers

The liquid break-up phenomenon can be characterised by several non-dimensional numbers, depending on the dominating mechanisms involved. These numbers express the relative importance of two or more of the involved processes: the Reynolds Re, Weber We and Ohnesorge Oh numbers, which are defined in Eqs. (2.1), (2.10) and (2.11). The Weber number describes the ratio between inertia and surface tension forces

whereas the Ohnesorge number involves the relation between viscous stress to inertial and surface tension forces.

$$We = \frac{\rho U^2 L}{\sigma} \tag{2.10}$$

$$Oh = \frac{\mu}{\sqrt{\rho \sigma L}} \tag{2.11}$$

The ratio of the liquid and gas density ρ_l/ρ_g and the ratio of the liquid and gas viscosity μ_l/μ_g are also important dimensionless parameters. σ denotes the liquid surface tension. As spray injection involves a large range of scales, different types of Re, We and Oh numbers can be established for characterising the flow under consideration.

2.3 Liquid Jets and Sprays

2.3.1 Liquid Jet Regimes

This work focuses on flow regimes of atomizing jets and sprays, see Fig. 2.3, that occur typically if fuel is injected in a combustion chamber. In

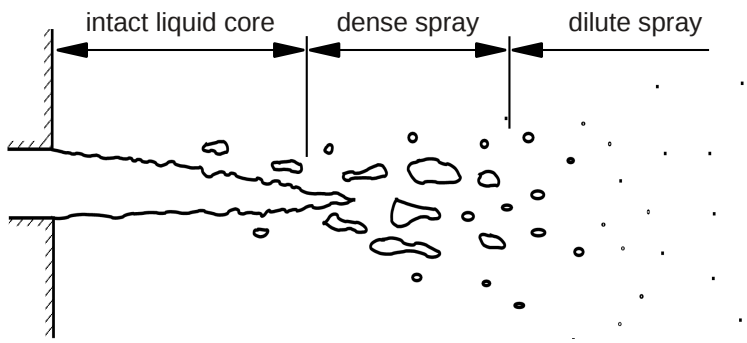

Figure 2.3: Atomizing jet and spray regimes.

a very small region directly at the nozzle an *intact liquid core* exists. Due to instabilities, ligaments and other irregular liquid structures are formed on the liquid core surface; this is called the primary breakup of

the jet. When the core is broken up, but the volume occupied by liquid compared to the volume occupied by gas within a certain region is still large, the flow regime is called *dense spray*. This is quantified by the liquid volume fraction α, defined as

$$\alpha = \frac{V_l}{V} = \frac{V_l}{V_l + V_g} \tag{2.12}$$

and the gaseous volume fraction θ, defined as

$$\theta = 1 - \alpha. \tag{2.13}$$

Here V_l and V_g are the volumes occupied by the liquid and gaseous phase, respectively, in a total volume V. The liquid structures break up into smaller droplets further downstream and the spray widens due to turbulent dispersion and gas entrainment whereby the liquid volume fraction decreases. When at some point the liquid volume fraction is small compared to the gaseous volume fraction, the flow regime is called a *dilute spray*. In this region the effects of individual droplets on neighbouring ones are small. The mean distance between droplets can be as much as 10-15 droplet diameters, which implies that the volume fraction is of the order of 0.1%. The dominant physical mechanisms are quite different depending on the flow regime: in a dilute spray the influence of droplets on each other is limited as stated above. Collisions are rare and a single droplet encounters a gas flow that is assumed to be undisturbed by other droplets. In a dense spray on the contrary, liquid structures are non-spherical, deformed, collide frequently and are affected by the other droplets. The surface to mass ratio is large for a dilute spray, which enhances evaporation processes, while this can be neglected for the liquid core and dense spray regimes [4]. These dominant mechanisms are crucial for the choice of models and corresponding numerical tools, as described in Ch. 4, 5 and 7.

The boundary between the dense and dilute spray regimes is not distinct. A dense spray is often assumed if the droplet spacing is equal to the droplet diameter, which, for a uniformly distributed monodisperse spray, results in a liquid volume fraction of $\alpha \approx 0.08$. In [33], the effect of a particle on the drag force acting on an identical following particle has been studied numerically: in tandem configuration the following particle

shows a reduction of 60%, 70% and 80% for droplet Reynolds numbers (Eq. (2.18)) of 50, 100 and 200 and a spacing equal to 6 times the particle diameter, which corresponds to $\alpha \approx 0.0024$. Thus, the conclusion is that wake effects are not significant (i.e. less than a few per cents) if the loading is lower by approximately an order of magnitude than the one given by [34] at $\alpha = 0.001$.

2.3.2 Flow and Droplet Timescales

A droplet is accelerated by the gas depending on its drag and mass: a large light droplet is following the turbulent eddy, while a small heavy droplet is not following the fluid due to the droplets inertia. Such behaviour can be characterised by the Stokes number,

$$St = \frac{\tau_d}{\tau_f}, \tag{2.14}$$

where τ_f is the local flow time scale and τ_d is the droplet response time.

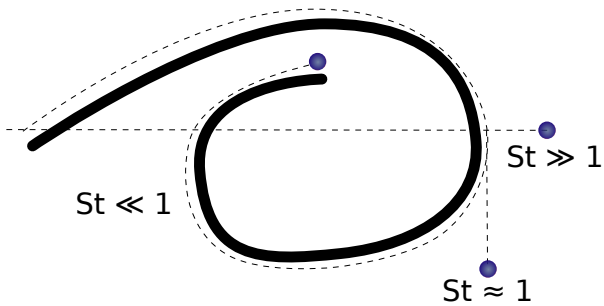

Figure 2.4: Vortex and possible droplet trajectories, after [35].

Therefore, a droplet with a small Stokes number will follow the fluid particle trajectory, whereas droplets with a large Stokes number will continue along their own path and will be less affected by the surrounding flow (see Fig. 2.4). This effect has been observed in [36].

The transfer of momentum from the flow to the droplets increases the momentum of the droplet and decreases the momentum of the eddy, thus, turbulence is damped by the droplets. On the other hand, large droplets may generate unsteady wakes which, in turn, enhance the local

fluctuation of the gas and thereby turbulence is enhanced. For the case of large Stokes numbers, the droplets leave the eddy within a short time. Therefore, there is a non-negligible momentum transfer between the two phases for all Stokes numbers that are not very small. It is also evident that turbulence will be dampened by the small droplets only if the number of droplets is large. These relations have been shown experimentally by [37] for particle-laden channel flows for the Stokes numbers of $St = 0.18$ and $St = 0.93$ and for various mass loadings. The dampening of turbulence by particles has been simulated numerically by [38], who found the strongest attenuation in the energy containing range, which is reasonable as this turbulence range is responsible for turbulent mixing.

2.3.3 Breakup of a Liquid Jet

The breakup of the liquid jet is caused by instabilities controlled by aerodynamic forces acting on the jet surface, turbulent motions inside the liquid or cavitation. Thus, several relevant non-dimensional numbers (Eqs. (2.1), (2.10) and (2.11)) are defined for the liquid jet as follows:

$$Re_{jet} = \frac{U_{inj} d_{noz}}{\nu_l} \tag{2.15}$$

$$We_{jet} = \frac{\rho_g U_{inj}^2 d_{noz}}{\sigma} \tag{2.16}$$

$$Oh_{jet} = \frac{\mu_l}{\sqrt{\rho_l \sigma d_{noz}}} \tag{2.17}$$

where the indices l and g indicate properties of the liquid and gas phase, U_{inj} is the injection velocity and d_{noz} is the nozzle diameter.

For primary breakup four different jet breakup regimes can be differed: the Rayleigh (Fig. 2.5(a)), the first wind induced (Fig. 2.5(b)), the second wind induced (Fig. 2.5(c)) and the atomization regime (Fig. 2.5(d)).

The Rayleigh breakup regime is dominated by the liquid inertia forces and the surface tension. The primary breakup of the liquid jet occurs several nozzle diameters downstream and the produced droplets are larger than the nozzle diameter. If, for example, the injection velocity is increased, the jet will breakup in the first wind induced regime. Here, the

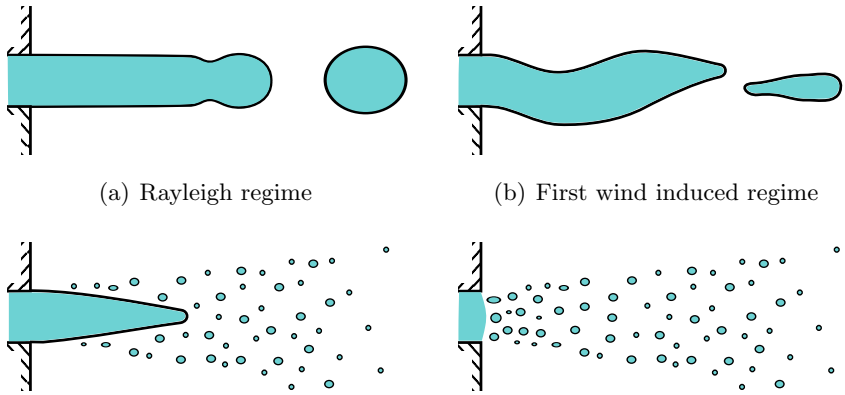

(a) Rayleigh regime (b) First wind induced regime

(c) Second wind induced regime (d) Atomization regime

Figure 2.5: Primary breakup regimes, after [39].

inertia of the gas phase becomes more important. The interaction between liquid and gas leads to a Rayleigh-Taylor instability, which causes the disturbances on the liquid surface to grow and the jet to break up. The breakup length is larger than the nozzle diameter and the resulting droplets are of a size of the order of the nozzle diameter. If the injection velocity is further increased the jet will break up in the second wind induced regime. The difference between the gas and liquid velocities increases and the excitement wavelengths decrease, which leads to Kelvin-Helmholtz instabilities. The breakup length and the droplet diameters are small compared to the first wind induced regime. If the injection velocity is large, the jet breaks up in the atomization regime, which is typical for Diesel engines. The liquid jet breakup length and the resulting droplets are very small. The mechanisms acting in the atomization regime are still not fully understood, as the primary breakup is difficult to measure in an experimental set-up in all breakup regimes, and especially in the atomization regime. It has been studied experimentally [4, 7], but as this region is optically dense, measurements are limited to identifying rather large liquid structures or more global parameters of the spray.

2.3.4 Breakup of Droplets

Due to interaction with the surrounding gas, aerodynamic forces destabilise and distort the droplet until it breaks up. Thus, the non-dimensional numbers (Eqs. (2.1), (2.10) and (2.11)) are defined for a droplet as

$$Re_d = \frac{U_{rel} d_d}{\nu_l}, \tag{2.18}$$

$$We_d = \frac{\rho_g U_{rel}^2 d_d}{\sigma}, \tag{2.19}$$

$$Oh_d = \frac{\mu_l}{\sqrt{\rho_l \sigma d_d}}, \tag{2.20}$$

where U_{rel} is the relative velocity between the droplet and the surrounding gas and d_d is the droplet diameter.

For secondary breakup, several different breakup regimes have been found experimentally [40], five of them are shown in Fig. 2.6: These include the vibrational, bag, bag/streamer, stripping and catastrophic breakups.

The droplet Weber number is an important parameter for determining the breakup regime that is applicable for the droplet. For small Weber numbers of about 12, vibrational breakup (Fig. 2.6(a)) occurs, due to droplet vibration until at some point it breaks up into two droplets of similar sizes. For a slightly higher Weber number of up to 20, bag breakup (Fig. 2.6(b)) may occur. The droplet is distorted into a bag shape until it breaks up, which results in a large number of small droplets and some larger droplets which originate from the rim of the bag. For Weber numbers up to 50, the droplet breaks up in the bag/streamer breakup regime (Fig. 2.6(c)). It is similar to the bag breakup regime, but here a streamer is formed inside the bag, which leads to some droplets of a larger size after breakup. For Weber numbers up to 100, stripping breakup (Fig. 2.6(d)) occurs. A large number of small droplets are stripped away from the surface of the droplet, due to aerodynamic forces on the drop surface. The droplet reaches catastrophic breakup regime (Fig. 2.6(e)) for Weber numbers larger than 100 and, due to the large slip velocity, a large number of small droplets are formed. In a typical fuel spray all these different regimes may be observed. Close to the nozzle the droplet diameters and

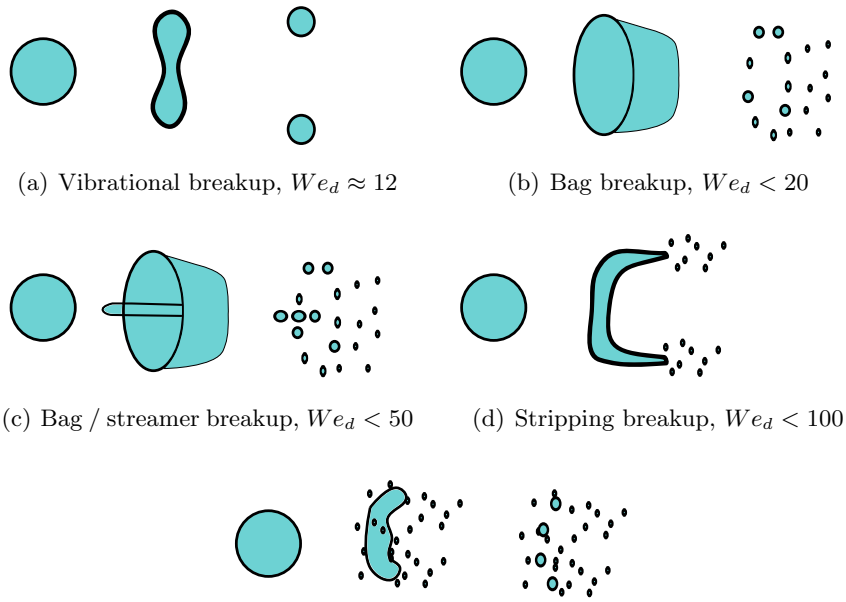

(a) Vibrational breakup, $We_d \approx 12$

(b) Bag breakup, $We_d < 20$

(c) Bag / streamer breakup, $We_d < 50$

(d) Stripping breakup, $We_d < 100$

(e) Catastrophic breakup, $We_d > 100$

Figure 2.6: Secondary droplet breakup regimes, after [40].

the gas-liquid relative velocity and therefore the Weber number are the largest, thus the catastrophic breakup regime may be dominant. For modern Diesel engine injectors, one uses high injection pressures (several thousand atmospheric pressure) leading to catastrophic breakup of the liquid jet into a large number of small droplets. In low pressure injectors further downstream of the nozzle the droplets get smaller due to further breakup, whereby the ambient gas gains momentum as the droplets decelerate. Consequently, the droplet Weber number is reduced and all the other breakup regimes might be seen.

2.3.5 Evaporation and Mixing

A mixture is a system of two substances that are not chemically combined, independently of their state. If the composition of the mixture

(i.e. the concentration) is uniform, it is called homogeneous, if not it is called heterogeneous. If a concentration is non-uniform initially, the mixture may become more homogeneous through molecular diffusion and primarily through turbulent mixing. Thus, if the spray is broken up into very fine droplets, it can mix with the gas and form an aerosol. However, the system mixes faster and more homogeneously if the liquid evaporates. In this case a single-phase flow is present and surface tension forces do not need to be overcome. Evaporation is the phenomenon of liquid mass that changes phase at the droplet surface and that is transported away from the surface. It is caused by the vapour concentration difference between the droplet surface and the free stream.

The mechanisms of mixing are the random motion of molecules, called molecular diffusion, and the transport of molecules due to flow convection. Due to its randomness and its three dimensional behaviour, the transport of properties due to turbulent fluctuations is the dominant mixing mechanism. Thus, beside deforming the liquid jet and the spray droplets and hence enhancing their breakup, turbulence in the gas phase also enhances the liquid-gas mixing.

Liquid-gas mixing is an important process in many industrial applications and essential for combustion applications: To reduce exhaust emissions one wishes the liquid fuel to be well mixed with the surrounding gas. As the available time and space, e.g. in a Diesel engine, is limited, fast mixing is required. On the other hand too fast mixing can lead to a too lean mixture. Thus, a fast but controlled mixing process is desired.

2.3.6 Pulsed Liquid Injection

Pulsed fuel injections were studied in the engine industry in the beginning with the purpose to create stratified cylinder charges. However, it was observed that enhanced mixing is attained at the end of the injection pulse. This effect has been studied experimentally [41, 42] for a pulsed gas jet. Hot wire probes were located at several downstream positions of the jet. When the velocity profiles at two monitoring points are compared, a time delay between the arrival of the pulse head at the first and the second point can be observed, which obviously corresponds to the jet

injection velocity. When comparing the arrival time for the pulse tails it is observed that the delay is less than for the head, in these measurements the delay was reduced by the factor 2. Thus, the tail of the pulse moves faster downstream than the head which results, due to mass conservation, in an increased air entrainment and indicates the formation of a entrainment wave that travels faster than the jet itself.

In [43] an analytical model was developed based on the simplified Navier-Stokes equations: a one-dimensional single-phase jet was considered, incompressibility was assumed and only the transient and convective terms in the momentum equations were taken into account. This model confirms the above described experimental results including the ratio of 2 between the pulse head and tail time delays. In [44] a CFD simulation was performed, using the two dimensional, compressible form of the Navier-Stokes equations for a single-phase jet, which also reconfirms the above results.

The effects of pulsed injection can also be observed in natural jets: there are objects in space, e.g. young stars, compact objects or galactic supermassive black holes, that generate astrophysical jets [45–47]. These jets consist of mass, momentum, energy or magnetic fluxes that are transported either through the interstellar or the intergalactic ambient medium. These jets have been modelled experimentally [48] and numerically [49]. Despite the fact that the properties of these kinds of jets are of a complete different parameter range than the above described fuel jets, similar features could be observed: the tail of the jet pulse moves with a different speed than the head. In this case it was observed that the tail moves faster for jets that are denser than the ambient medium and slower for jets that are less dense than the ambient medium.

CHAPTER 3

EQUATIONS OF SINGLE-PHASE FLOWS

3.1 Navier-Stokes Equations

The flow of Newtonian fluids, i.e. a fluid whose stress versus strain rate is linear, is described by the Navier-Stokes equations, independently of their aggregate state. They were formulated independently by the Irish mathematician George Gabriel Stokes in 1827 and the French mathematician Claude Louis Marie Henri Navier in 1843. Strictly speaking, the Navier-Stokes equations name the momentum conservation equations for incompressible fluids. However, commonly also the mass and energy conservation equation are referred to as Navier-Stokes equations and form thus, the governing equations for the motion of Newtonian fluids. The starting point for each equation is a physical principle describing the conservation of a quantity: the mass conservation equation applies the assumption that mass can neither be created nor destroyed, while the momentum conservation equation extends Newtons second law of motion to fluids and the energy conservation equation is derived from the first law of thermodynamics, saying that the total amount of energy is constant. All three physical principles are valid for isolated systems. For the purpose of CFD, the Reynolds transport theorem is applied to derive the conservation equations for a finite control volume fixed in space.

Assuming incompressibility and if instead of a control volume of a finite size, an infinitely small control volume is assumed, the Navier-Stokes equations in differential form are obtained (Eqs. (3.1) - (3.3)).

$$\frac{\partial u_i}{\partial x_i} = 0 \tag{3.1}$$

$$\rho\frac{\partial u_i}{\partial t} + \rho u_j\frac{\partial u_i}{\partial x_j} = -\frac{\partial p}{\partial x_i} + \frac{\partial \tau_{ij}}{\partial x_j} \tag{3.2}$$

$$\rho c_p\frac{\partial T}{\partial t} + \rho c_p u_j\frac{\partial T}{\partial x_j} = \rho c_p D_{th}\frac{\partial T}{\partial x_j \partial x_j} + \tau_{ij}\frac{\partial u_i}{\partial x_j} \tag{3.3}$$

The equations are written, as well as the following equations in this work using the Einstein summation convention. ρ is here the density of the fluid, u the velocity, the index i gives for the coordinate direction and t denotes the time, p corresponds to the static pressure, τ_{ij} to the viscous stresses, T is the temperature, D_{th} the molecular thermal diffusion coefficient and c_p the specific heat under constant pressure. On the left hand side of the momentum equation, the first term gives the unsteady and the second term the convective acceleration of the fluid. On the right hand side of the momentum equation, the first term corresponds to the pressure gradient and the second to the viscous stress gradient. On the left hand side of the energy equation, the first term gives the unsteady and the second term the convective heat transfer of the fluid. On the right hand side, the first term accounts for heat conduction and the second term for viscous work. These equations are reduced or extended in the following chapters to be valid for certain flow situations and might be closed by the equation of state.

Analytical solutions for the above equations are so far only found for special, very simplified flow cases. Thus, to determine the flow field, one needs to perform experiments or, as done in the present work, numerical simulations. So far the existence of a solution has been proven only for small Reynolds numbers. Due to their great importance, the Clay Mathematics Institute included the proof of the "existence and smoothness of the Navier-Stokes equations" to the "Millenium Prize Problems", the seven most important unsolved problems in mathematics and will reward the solution or a counter example with one million Dollar [50].

3.2 Turbulence Modelling

Turbulent flows of sufficiently high Reynolds numbers contain a wide range of scales in time and space, as described in Ch. 2.1.3. Resolving all scales results in a challenging task in terms of computational work. Therefore, techniques have been developed to model turbulence instead of resolving it.

Direct Numerical Simulation

As no models, averaging or filtering is needed, Direct Numerical Simulation (DNS) is the easiest to implement and the most exact method to simulate turbulence. All turbulent scales are resolved. Thus, the domain size has to be at least the size of the largest turbulent structure, l_0, and the cell size not larger than the smallest turbulent structure, l_η. Therefore the number of grid points in each direction scales, according to Eq. (2.9), with $Re^{3/4}$. As the timestep is linearly related to the cell size, the computational effort scales with Re^3. Thus, DNS is today limited to small domains and low Reynolds number flows and not feasible for industrial applications.

Reynolds-averaged Navier-Stokes Equations

The dependent variables may be averaged in space, time, or over an ensemble of data. The different averaging approaches may lead to different results. If the Navier-Stokes equations are averaged over time, the Reynolds-averaged Navier-Stokes (RANS) equations are obtained. This is often a reasonable approach as for many problems only time averaged quantities are of interest and not their turbulent fluctuations. For a statistically stationary flow, the flow quantity ϕ can be decomposed in its time average $\langle\phi\rangle$ and its fluctuations ϕ' as follows:

$$\phi(x,t) \;=\; \langle\phi(x)\rangle + \phi'(x,t) \tag{3.4}$$

The time average of ϕ is defined as

$$\langle\phi\rangle \;=\; \lim_{\tau\to\infty}\frac{1}{\tau}\int_0^\tau \phi(x,t)dt \;, \tag{3.5}$$

where τ is a time interval that has to be long enough so that the average is independent of τ. If the flow contains slow variations that can be separated from the turbulent spectrum, the averaging time can be smaller then the timescale of the variation of the mean but larger than all the turbulent timescales. This averaging leads to the RANS equations for the mean flow:

$$\frac{\partial \langle u_i \rangle}{\partial x_i} = 0 \tag{3.6}$$

$$\rho \frac{\partial \langle u_i \rangle}{\partial t} + \rho \langle u_j \rangle \frac{\partial \langle u_i \rangle}{\partial x_j} = -\frac{\partial \langle p \rangle}{\partial x_i} + \frac{\partial \langle \tau_{ij} \rangle}{\partial x_j} - \rho \frac{\partial \langle u_i' u_j' \rangle}{\partial x_j} \tag{3.7}$$

Due to the averaging, a new term, $\rho \frac{\partial \langle u_i' u_j' \rangle}{\partial x_j}$, arises on the right hand side of the momentum equation, the so-called *Reynolds stresses*. As the turbulent velocity fluctuations u_i' are unknowns the system of equations is not closed. To close the equations some expressions, called turbulence models, need to be introduced. This is usually done by expressing values for the Reynolds-stress term as functions of the flow variables. For flows that are not statistically stationary, one uses ensemble averaging. The resulting equations are the same as for the time averaged ones, though the averaging means different things in the two cases.

The RANS equations are relatively easy to solve and are applicable to general turbulent flows that satisfy the assumption used in their derivation and the derivation of Reynolds-stress model. Therefore, the RANS framework is most commonly used in industrial applications. The main limiting factors for the RANS modelling is the turbulence models themselves and the handling of the near wall region. When comparing their performances in a wide range of test flows, they often fail for flow situations that are somewhat different from the ones they have been calibrated for. Examples are the Baldwin-Lomax mixing-length model [51] or the standard $k - \epsilon$ model [52], which both perform well for flows over wings, but according to [53] no quantitative agreement to experimental data for oscillating wings. In [54], the standard $k - \epsilon$ model and the Reynolds-stress model show not to resolve sufficiently the transient mixing processes of the air in urban streets, because the unsteady fluctuations of the flow field are not well captured.

Large Eddy Simulation

Large Eddy Simulation (LES) is based on space-averaging. Since the character of the averaging is not explicitly utilised in the derivation of the averaged Navier-Stokes equations above, the averaged governing equations are formally alike the ones for the ensemble and time averaging. The crucial and important effect of the different types of averaging manifests in the new non-linear term. In the RANS framework the divergence of the terms are called, as is stated above, the Reynolds-stresses. The corresponding terms in the LES framework are called the Sub-Grid-Scale (SGS) terms. Modelling these terms has been a subject of research for several decades. The rationale of the LES and SGS modelling stems from Kolmogorov's theory (see Ch. 2.1.2). The large, problem dependent turbulent structures are resolved, while the small scale structures are universal and their influence can therefore be modelled. This is reasonable, as most of the energy and anisotropy are contained in the large scale motions which are resolved in LES. In contrast, most of the computational effort in DNS is spend to solve the small scale motions. Due to the need for better spatial resolution, LES is computationally more expensive than RANS but less expensive than DNS. As only the larger scales are resolved, a spatial filter function G is applied to the flow field variables, as shown here for a generic variable ϕ:

$$\overline{\phi}(x) \;=\; \int G(x-r)\phi(r)dr \tag{3.8}$$

The filtered quantities are denoted by an overline. The exact form of the filter function is not entering into the equations, though they may enter into the SGS model. Applying this filter leads to the spatially filtered Navier-Stokes equations:

$$\frac{\partial \overline{u}_i}{\partial x_i} \;=\; 0 \tag{3.9}$$

$$\rho\frac{\partial \overline{u}_i}{\partial t} + \rho\overline{u}_j\frac{\partial \overline{u}_i}{\partial x_j} \;=\; -\frac{\partial \overline{p}}{\partial x_i} + \frac{\partial \overline{\tau}_{ij}}{\partial x_j} - \rho\frac{\partial(\overline{u_i u_j} - \overline{u}_i\overline{u}_j)}{\partial x_j} \tag{3.10}$$

For spatial filtering, in contrast to time averaging, $\overline{u_i u_j} \neq \overline{u}_i\overline{u}_j$. Here, as in the case of the Reynolds stress, the last (SGS) term on the right

hand side of the momentum equation can not be derived from the filtered quantities. Therefore, the system of equations is not closed and the term needs to be modelled. One may show that a standard (e.g. central second order) finite-difference approximation to a spatial derivative acts as a top-hat filter with a length proportional to the grid size.

In general, the turbulence model used is not as crucial for LES as it is for RANS, as most of the energy is resolved and only the small scale motions are modelled, while in RANS the turbulent fluctuations of all scales are modelled. If the Kolmogorov spectrum is integrated to the smallest scales, the unresolved energy reduces by the smallest scale to power 2/3. Thus, when refining the grid the unresolved energy diminishes. When the filter size is reduced to or below the size of Kolmogorov eddies, LES converges to DNS.

There are several models proposed to close the filtered equations. Some of the most popular ones are the Smagorinsky model [55], Germano's dynamic model [56] or Bardina's scale similarity model [57]. All of them suffer of certain problems: all assume the correlation between the filtered rate of strain and the residual stresses, which has been shown in experiments [58] to be weak. By the nature of its equations, the Smagorinsky model can give only positive values for the residual stresses. Therefore, it does not account backscatter and it is incorrect for laminar flow, which can lead to an over-prediction of dissipation.

The main role of the SGS terms are to account for the dissipation on small scales and to represent the effects of the unresolved scales on the resolved ones. Thus, an SGS model has to exhibit some dissipation either explicitly or implicitly through the numerical scheme (i.e. discretization). In this work the 'implicit model' is employed, that means no explicit SGS expression is used. By not including explicit dissipation, the overall dissipative properties of the discrete system are reduced. When the governing equations are discretized (see Ch. 6), numerical errors are introduced out of which the spatial truncation error is dominant. For the linearised Navier-Stokes equations one may show that the truncation error has to be dissipative in order to ensure convergence of the iterative algorithm. It was claimed in [59] that instead of using an explicit residual stress model, an appropriate numerical method should be used so that the numerical stress accounts for the dissipation of the small scales.

An advantage of this method is that the implementation is simple. A disadvantage is that the modelling and the numerics are not independent of each other. It must be emphasised that one may rely on such a model only if the resolution is fine enough so that a considerable part of the turbulence energy spectrum is resolved, i.e. the computational grid is fine enough. According to Kolmogorovs third similarity hypothesis, the spatial resolution must be such that the inertial sub-range is resolved. Thereby, the effects of dissipation (numerical or molecular) are not observed in the resolved scales and therefore the effect of the SGS terms on the resolved scales can be neglected.

CHAPTER 4

EQUATIONS OF LIQUID JETS

4.1 Governing Equations

Ch. 2.3.3 concludes that the interaction of a liquid jet with a surrounding gas is strong, which leads to the breakup of the jet. The resulting spray is dense with strong interactions among the droplets, including collisions and coalescence. Interaction with the surrounding gas leads to droplet deformation and further breakup. As it can be concluded from Ch. 2.1.3, that the droplets will generate turbulence in the gaseous phase with scales that are about one order smaller than the droplet itself. Also the liquid structures are of an irregular shape and cannot be handled by simple breakup models that describe spherical or slightly distorted spherical droplets. Therefore, to resolve the turbulent structures in the gas phase, the shape of the liquid structures and the flow inside the liquid, the VOF method is used in the intact liquid jet and dense spray regime. As stated in Ch. 2.3.1, evaporation may be neglected in these regimes at temperatures which are not very high, as the ratio of liquid surface to liquid mass is small. The gas and liquid phase can be considered as incompressible, but as their densities may be very different, thus, the density of the mixture will change in time and space. Therefore, the flow field is described in Eulerian framework by the isothermal, compress-

ible Navier-Stokes equations for multiphase flows without phase changes, where the density is only dependent on the species, but independent of the pressure. The non-dimensional equations are given in Eqs. (4.1) and (4.2).

$$\frac{\partial \rho}{\partial t} + \frac{\partial u_i \rho}{\partial x_i} = 0 \tag{4.1}$$

$$\frac{\partial u_i \rho}{\partial t} + u_j \frac{\partial u_i \rho}{\partial x_j} = -\frac{\partial p}{\partial x_i} + \frac{1}{Re_{jet}} \frac{\partial}{\partial x_j} \left(\mu \left(\frac{\partial u_i}{\partial x_j} + \frac{\partial u_j}{\partial x_i} \right) \right) + \frac{\kappa \delta n_i}{We_{jet}} \tag{4.2}$$

The last term on the right hand side of the momentum equation represents the surface tension, where δ is a Dirac function which is unity at the interface and zero elsewhere, κ is the interface curvature and n_i the interface unit normal. Re_{jet} and We_{jet} are defined in Eqs. (2.15) and (2.16), the density and the viscosity are calculated linearly dependent on the phase variable α, see Eqs. (4.3) and (4.4).

$$\rho = \rho_g + (\rho_l - \rho_g)\tilde{\alpha} \tag{4.3}$$

$$\mu = \mu_g + (\mu_l - \mu_g)\tilde{\alpha} \tag{4.4}$$

α describes the volume fraction according to Eq. (2.12). $\tilde{\alpha}$ is a smoothed form of α using a smoothing function described by Rudman [60]. When introducing Eq. (4.3) in Eq. (4.1), one obtains

$$(\rho_l - \rho_g) \left(\frac{\partial \alpha}{\partial t} + \frac{\partial u_i \alpha}{\partial x_i} \right) + \frac{\partial u_i \rho_g}{\partial x_i} = 0 \ . \tag{4.5}$$

Introducing Eq. (4.15) in Eq. (4.5) sets the left term to 0 and leads to the incompressible form of the mass conservation equation :

$$\frac{\partial u_i}{\partial x_i} = 0 \tag{4.6}$$

The left hand side of the compressible momentum conservation equation can be written as

$$\rho\frac{\partial u_i}{\partial t} + u_i\frac{\partial \rho}{\partial t} + \rho u_j\frac{\partial u_i}{\partial x_j} + u_i u_j\frac{\partial \rho}{\partial x_j} = \cdots \ . \tag{4.7}$$

Inserting the incompressible (Eq. (4.6)) into the compressible (Eq. (4.1)) mass conservation equation leads to

$$\frac{\partial \rho}{\partial t} + u_i\frac{\partial \rho}{\partial x_i} = 0 \ . \tag{4.8}$$

When introducing this into Eq. (4.7), the incompressible form of the momentum equation is obtained:

$$\rho\frac{\partial u_i}{\partial t} + \rho u_j\frac{\partial u_i}{\partial x_j} = -\frac{\partial p}{\partial x_i} + \frac{1}{Re_{jet}}\frac{\partial}{\partial x_j}\left(\mu\left(\frac{\partial u_i}{\partial x_j} + \frac{\partial u_j}{\partial x_i}\right)\right) + \frac{\kappa\delta n_i}{We_{jet}} \tag{4.9}$$

4.2 Surface Tension Modelling

Unbalanced cohesive forces at the liquid gas interface lead to surface tension forces, which can be written as

$$F \ = \ \kappa\sigma \ . \tag{4.10}$$

When this expression is multiplied by δn_i it gives the right direction and is applied to the right computational cell. Its non-dimensional form is equal to the last term in Eq. (4.9). According to the Continuum Surface Force (CSF) model as described in [61], the Dirac function and the interface unit normal are replaced by

$$\delta n_i \ = \ \frac{\partial \alpha}{\partial x_i} \ . \tag{4.11}$$

The normal direction of the interface, which is needed later for the phase transport and the curvature, is estimated from the α field using the Direction Averaged Normal (DAN) model [62]. To reduce the computational effort, the calculations are carried out in the direction of the largest component of the normal vector. A distance function, Λ, is introduced which is estimated based on the volume fractions of the neighbouring

cells. These volume fractions are summed up in the calculation direction. It gives the distance of the interface in the neighbouring cells to the centre of the current cell. For the z-direction this leads to the following expressions for the interface normal:

$$n = \begin{pmatrix} n_x \\ n_y \\ n_z \end{pmatrix} = \frac{\frac{\partial \alpha}{\partial x_z}}{|\frac{\partial \alpha}{\partial x_z}|} \cdot \begin{pmatrix} -\frac{\partial \Lambda}{\partial x_x} \\ -\frac{\partial \Lambda}{\partial x_y} \\ 1 \end{pmatrix} \tag{4.12}$$

This procedure, as it considers only the largest normal component, is simpler and faster as comparable methods, such as [63, 64].

Finally, the curvature is calculated applying the Direction Averaged Curvature (DAC) model [65]. As for the DAN, the computational effort is reduced by carrying out the calculations in the direction of the largest normal component. In a similar way a distance function Λ is established. For the z-direction this leads to the following expressions for the interface curvature:

$$\kappa = \frac{n_z}{|n_z|} \left(\frac{\Lambda_{ii}}{|n|} - \frac{\Lambda_i \Lambda_j \Lambda_{ij}}{|n|^3} \right) \tag{4.13}$$

This procedure, as it considers only the largest normal component, is simpler and faster as comparable methods, such as [64].

The maximum error in the curvature when using this method has been investigated in [66] for a droplet under static equilibrium. It has been shown that, if the droplet is resolved by ten cells over the diameter, the maximum error for κ is approximately 4 %. As the Weber numbers in engines are usually large, the error originating from the surface tension term is considered to be small.

4.3 Motion of the Phase Interface

To apply the surface tension forces to the flow equations, as described in the previous chapter, the topology of the gas-liquid interface needs to be known. If phase transition such as evaporation is neglected, the surface position, x_s, is described as

$$\frac{dx_s}{dt} = u(x_s, t) \ . \tag{4.14}$$

Several methods have been proposed to describe the motion of the interface, which (following [67])can be grouped into *surface tracking methods* and *volume tracking methods*.

In surface tracking methods, the surface of the gas-liquid interface is tracked and the related liquid and gas volumes are derived from the position of the interface. One of these surface tracking methods is the *front tracking method* [68]. A number of marker particles, located on the interface, is defined and tracked in Lagrangian manner. The flow velocity is used to obtain the motion of these mass free particles. Flow solver grid points can be used as marker points, which ensures interface conforming flow solver grids, but requires remeshing for each interface topology change. The method is very accurate, with the disadvantage that interface topology changes need to be modelled. Another surface tracking method is the *level-set method* [69,70]. An additional scalar that describes the interface directly is solved. This gives a sharp interface, but the method is not mass conservative.

In volume tracking methods, the liquid and volume is tracked and the surface of the interface is reconstructed from that. This reconstruction is the main drawback of these methods. One of these volume tracking methods is the *marker and cell* (MAC) method [71]. Mass free marker particles are transported in Lagrangian manner with the flow field. From the presence of particles that mark liquid or gas, the presence of liquid or gas phase in a computational cell can be derived. This is very accurate, but due to a immense number of required particles computationally very expensive. Another volume tracking method is the VOF [72] method, which is significantly faster compared to the MAC method. In VOF, an additional scalar for the liquid volume fraction is solved from which the interface shape needs to be reconstructed. As this method is, in opposite to level-set methods, inherently mass conservative, it is the choice of this work to use the VOF method.

For the additional scalar, α, which represents the liquid volume fraction, the transport equation

$$\frac{\partial \alpha}{\partial t} + \frac{\partial u_i \alpha}{\partial x_i} = 0 \tag{4.15}$$

is solved. When solving this equation it is of utmost importance to be not too diffusive in order to keep the liquid gas interface sharp and to use a stable approach at the same time. Several approaches have been proposed and compared in [73] and [67]. In both works the ability to keep the interface sharp and the mass conserved has been studied with simplified advection and shear flow cases and a case capturing the progression of the Rayleigh-Taylor instability. In [73] the direction split method proposed by [74] is shown to superior to the Simplified Line Interface Calculation (SLIC) method [75], the original VOF method [72] and the flux-corrected transport (FCT) method proposed by [73]. In [67] the Lagrangian Piecewise Linear Interface Construction (PLIC) [76], the CICSAM [77] and the inter-gamma differencing scheme [78] are judged superior to the above mentioned FCT method. Based on the discussion above, the method proposed by [74], extended from 2D to 3D as done in [62], is applied in this work. This is done by using the method sequentially for each spatial direction, which is therefore called direction split method, during one timestep. For one direction the algorithm is the following:

1. For each cell containing an interface, the normal vector of the interface is estimated from the volume fraction field with the DAN method.

2. From the volume fraction and the normal vector, a plane representing the interface is reconstructed.

3. The outgoing fluxes are determined from the plane and the flow velocities.

The direction split method leads to the issue that after calculating one direction the volume fraction in the cell might be larger than unity. This can happen e.g. if the volume fraction before the calculation is already close to one and when considering only the first direction even more liquid is added. The volume fraction can than be higher than one,

as the outflow of the liquid in the second or third direction are not yet taken into account. Therefore, an effective cell volume is defined, which includes the cell volume before the calculation of the specific direction and additionally the fluid in- and outflow. The general expression for the effective volume, δV^m_{ijk}, is

$$\delta V^m = 1 - \Delta t \sum_{i=1}^{m} \frac{\Delta u_i}{h_i} , \tag{4.16}$$

where m defines the direction ($1 \leq m \leq 3$) calculated in the present sweep and Δu_i is the velocity difference between the cell edges in i-direction. The volume fraction for the timestep $n+1$ is given by

$$\alpha^{n+1,m} = \frac{\alpha^{n+1,m-1}\delta V^{m-1} - \Delta\Gamma^m}{\delta V^m} , \tag{4.17}$$

where $\Delta\Gamma^m$ is the flux difference of α in m-direction and the following definitions are valid:

$$\alpha^{n+1,0} = \alpha^n \tag{4.18}$$

$$\alpha^{n+1} = \alpha^{n+1,3} \tag{4.19}$$

CHAPTER 5

EQUATIONS OF DISPERSED FLOWS

A flow is called dispersed if one phase, i.e. the liquid phase, is not materially connected. To simulate the dilute spray regime, the continuous gas phase is described in Eulerian and the dispersed liquid phase in Lagrangian framework. As the droplets are small with relatively large inter-droplet distance, it is natural to consider the droplets being spherical (very small droplets become spherical due to surface tension), and not interacting with each other (i.e. no collision or history/wake effects). Since each droplet is small and the loading is small the total volume displaced by the droplets is small when compared to the volume occupied by the carrier gas. For this reason, it is also not rational to use VOF which requires resolving each individual droplet. The description of the liquid phase in Lagrangian framework is computationally much more efficient than in the VOF-Eulerian framework. Additionally, as the droplets tend to be spherical, it is easier to track them individually and to model the subsequent breakup and evaporation processes.

5.1 Continuous Phase

The continuous gaseous phase is described in the Eulerian framework by the mass, momentum, energy and mixture fraction transport equation

for Newtonian fluids. The dimensional equations are given in Eqs. (5.1) - (5.4). Low Mach number flow is assumed, which means that the density is a function of the temperature only. Thereby, acoustic effects are neglected. Due to the assumption of dilute spray, the continuous phase volume fraction θ is assumed to be unity.

$$\frac{\partial \rho_g}{\partial t} + \frac{\partial \rho_g u_j}{\partial x_j} = \dot{m}_S \tag{5.1}$$

$$\frac{\partial \rho_g u_i}{\partial t} + \frac{\partial \rho_g u_i u_j}{\partial x_j} = -\frac{\partial p}{\partial x_i} + \frac{\partial}{\partial x_j}\mu\frac{\partial u_i}{\partial x_j} + \dot{F}_{S,i} \tag{5.2}$$

$$\frac{\partial \rho_g T_g}{\partial t} + \frac{\partial \rho_g u_j T_g}{\partial x_j} = \frac{\partial}{\partial x_j}\rho_g D_{th}\frac{\partial T_g}{\partial x_j} + \dot{Q}_S \tag{5.3}$$

$$\frac{\partial \rho_g Z}{\partial t} + \frac{\partial \rho_g u_j Z}{\partial x_j} = \frac{\partial}{\partial x_j}\rho_g D_m\frac{\partial Z}{\partial x_j} + \dot{Z}_S \tag{5.4}$$

$\dot{m}_S$, $\dot{F}_{S,i}$, $\dot{Q}_S$ and $\dot{Z}_S$ are source terms for mass, momentum, energy and mixture fraction, which account for the coupling from the liquid to the gaseous phase.

The gas density is assumed not to depend on pressure changes, but only on temperature variations. Hence, the system of equations is closed by the equation of state for incompressible, non-isothermal flows:

$$p_0 = \rho_g R T_g, \tag{5.5}$$

where p_0 is the constant reference pressure.

5.2 Dispersed Phase

The dispersed phase is described by the stochastic parcel method and the droplet probability distribution function is given by Eq. (5.6).

$$f(\vec{x}, \vec{u}_d, d_d, T_d, y, \dot{y}) d\vec{x}\, d\vec{u}_d\, dd_d\, dT_d\, dy\, d\dot{y} \tag{5.6}$$

The droplet distribution function gives the statistical number of droplets that are present between $\vec{x}$ and $\vec{x}+d\vec{x}$, of a speed between $\vec{u}_d$ and $\vec{u}_d+d\vec{u}_d$, of a diameter between d_d and $d_d + dd_d$, of a temperature between T_d

and $T_d + dT_d$ and of distortion parameters between y and $y + dy$ and the distortion rates $\dot{y}$ and $\dot{y}+d\dot{y}$. The complete number of droplets is gathered in parcels each representing the corresponding number of droplets, f. Each parcel is considered as a particle and tracked individually in the Lagrangian particle tracking framework.

In this approach the interface between the liquid phase and the gaseous phase is not resolved. Instead the flow properties are averaged over a larger distance than the diameter of the droplets. Thus, models are needed that describe the processes that act on the surface. These models are discussed in the following sections.

5.2.1 Momentum Exchange

Aerodynamic Drag Force

Only aerodynamic drag is taken into account for the momentum exchange between gaseous and liquid phases. The acceleration of a spherical, isolated, rigid droplet is according to Newton's second law of motion

$$\frac{d\vec{u}_d}{dt} = -\frac{3\rho_g}{4\rho_l d_d} C_w |u_{rel}| u_{rel} \ , \tag{5.7}$$

where C_w is the drag coefficient of the droplet. Following [79], C_w is defined depending on the droplet Reynolds number (Eq. (2.18)) as :

$$C_w = \frac{24}{Re_d}(1 + \frac{1}{6} Re_d^{2/3}) \qquad \text{for } Re_d \leq 1000 \tag{5.8}$$

$$C_w = 0.424 \qquad \text{for } Re_d \geq 1000 \tag{5.9}$$

Thus, the drag coefficient for the droplet follows the standard drag curve for a sphere. The influence of droplet deformation on the drag and resulting lift forces is not taken into account. The effect of the non-sphericity of particles has been studied in [80] using DNS: for example for $Re_d = 300$, the drag coefficient of an ellipsoid with the ratio of the longest to the smallest semi-axis of 5/4 raises by up to 20 % (depending on the orientation to the flow) compared to the drag coefficient of a sphere. For an ellipsoid with the ratio of the longest to the smallest semi-axis of 5/2, the drag coefficient lowers by up to 37 % and raises

up to 75 % depending on the flow orientation. As here the droplets are considered small and, thus, spherical, this effect is neglected.

From Eqs. (5.7) and (5.8) the force acting on a droplet follows as :

$$\vec{F}_d \;=\; m_d \cdot \frac{d\vec{u}_d}{dt} \tag{5.10}$$

Other Forces

There are other forces acting on the droplet, which are neglected in the current work. The sum of all forces result in the inertial force, which is balanced by the droplet mass times its acceleration,

$$\vec{F}_{in} \;=\; \frac{\pi}{6} d_d^3 \rho_l \frac{d\vec{u}_d}{dt} \;. \tag{5.11}$$

When a droplet is accelerated, parts of the surrounding gas are dragged with the droplet due to viscous effects. The force that is required for accelerating the surrounding fluid is called *virtual mass force*, F_{vm}, which equals [81]

$$\vec{F}_{vm} \;=\; \frac{\pi \rho_g d_d^3}{12} \left(\frac{D\vec{u}}{Dt} - \frac{d\vec{u}_d}{dt} \right) \;, \tag{5.12}$$

where $\frac{D\vec{u}}{dt}$ is the substantial derivative of the gas velocity and $\frac{d\vec{u}_d}{dt}$ is the droplet acceleration. The order of the ratio between both can, according to [82], be approximated by

$$\frac{\frac{D\vec{u}}{Dt}}{\frac{d\vec{u}_d}{dt}} \;\approx\; \frac{\frac{d\vec{u}}{dt}}{\frac{d\vec{u}_d}{dt}} \;\approx\; (St + 1) \;. \tag{5.13}$$

Using this relationship, the ratio between inertial force and virtual mass force can be estimated to be

$$\frac{\vec{F}_{vm}}{\vec{F}_{in}} \;\approx\; \frac{\rho_g}{\rho_l} \left(\frac{\frac{D\vec{u}}{Dt}}{\frac{d\vec{u}_d}{dt}} - 1 \right) \;\approx\; \frac{\rho_g}{\rho_l} St \;. \tag{5.14}$$

Thus, for small droplets with rather small Stokes numbers and for flows with high liquid-gas density ratio (both are expected in the dilute spray regime) the ratio of the virtual mass and the inertial force is of the order

of the gas-liquid density ratio. In the current work the gas-liquid density ratio is between 2% and 10%.

The relation for the aerodynamic drag, Eq. (5.7), and for the drag coefficient for $Re_d \leq 1000$ is derived analytically assuming an uniform gas flow. If the flow around the droplet is non-uniform, i.e. the droplet size is not small compared to the scale of the local gradients, the *Faxen force*, F_{fax}, is added as a correction. As stated earlier, we expect the turbulent scales in the dilute spray regime to be one order larger than the droplet diameters, thus, the flow around droplets can be considered uniform and Faxen forces can be neglected. The time delay in building up a boundary layer is reflected in the *Basset history* term. *Saffman forces* are caused by the rotation of droplets which is due to large velocity gradients in shear flows. In the cases considered here, the distance between the droplets and the walls is large enough to allow the assumption of neglecting the Saffman force. Assuming that the droplets do not rotate allows also to neglect the *Magnus force*. In this work, as in most other spray simulations, the mentioned forces as well as *gravitational forces* are neglected. This is justified in [82].

5.2.2 Secondary Breakup Models

Due to the different mechanisms that may occur at different breakup regimes, different models have been developed to describe the various secondary breakup types. In this work, breakup models for the two breakup regimes are used, which are assumed to be dominating: the bag breakup and the stripping breakup regimes. Following [83], break up is modelled by the Wave Breakup Model as long as the droplets contain more than 95% of the initially injected mass. If the droplet has less than 95% of the injected mass it is modelled by the Taylor Analogy Breakup (TAB) Model. Both breakup models are briefly described in the following.

Wave Breakup Model

The Wave breakup model according to [84] describes the stripping breakup and the bag breakup regime.

Stripping Breakup

Experimental findings show that a droplet is unstable in this regime when its Weber number (Eq. (2.19)) exceeds the square root of the droplet Reynolds number (Eq. (2.18)),

$$We_d > \sqrt{Re_d} \ . \tag{5.15}$$

The lifetime of an unstable droplet is given as

$$t_{strip} = C_1 \frac{d_d}{2 \cdot u_{rel}} \sqrt{\frac{\rho_l}{\rho_g}} \ . \tag{5.16}$$

In this work the parameter C_1 is set to 20 according to [84]. The diameter of the new stable droplet follows from the breakup criterion of Eq. (5.15) to

$$d_{stable} = \frac{\sigma^2}{\rho_g^2 u_{rel} \nu_l} \ . \tag{5.17}$$

From the initial droplet diameter and d_{stable}, the stripped away mass can be computed.

Bag Breakup

Experimental findings and theoretical considerations show that a droplet is unstable in this regime when its Weber number is larger than 12,

$$We_d > 12 \ . \tag{5.18}$$

The lifetime of an unstable droplet is given by

$$t_{bag} = C_2 \sqrt{\frac{\rho_d d_d^3}{8\sigma}} \ . \tag{5.19}$$

In this work the parameter C_2 is set to $\pi/\sqrt{2}$, according to [85]. The diameter of the new stable droplet follows from the breakup criterion of Eq. (5.18) to

$$d_{stable} = \frac{12\sigma}{\rho_g u_{rel}^2} \ . \tag{5.20}$$

The new droplets are assumed to be all of the same size, namely with a diameter of d_{stable}. From mass conservation and the original droplet number $N_{unstable}$ and diameter $d_{unstable}$, the number of newly created droplets follows directly to

$$N_{stable} = \frac{N_{unstable} d_{unstable}^3}{d_{stable}^3} \ . \tag{5.21}$$

Taylor Analogy Breakup (TAB) model

The TAB model according to [86] describes the bag breakup regime. It uses the analogy between a distorted droplet and a spring-mass system, for which the movement is generally given by a second-order differential equation

$$m\ddot{x} + b\dot{x} + \varsigma x = F \ , \tag{5.22}$$

where m is the mass, b the damping constant, ς spring constant, F the external force and x the distortion of the spring. When defining the analogy to the droplet, F can be interpreted as the aerodynamic force acting on the droplet, the liquid viscosity acts as a damping, the surface tension as a restoring force and the spring distortion corresponds to the distortion parameter of the droplet, y. Thus, the following substitutions can be made:

$$\frac{F}{m} = C_3 \frac{\rho_g u_{rel}^2}{\rho_l d_d} \tag{5.23}$$

$$\frac{\varsigma}{m} = C_4 \frac{\sigma}{\rho_l d_d^3} \tag{5.24}$$

$$\frac{b}{m} = C_5 \frac{\mu_l}{\rho_l d_d^2} \tag{5.25}$$

$$x = y \cdot C_6 \cdot d_d \tag{5.26}$$

This leads to the distortion equation of the droplet,

$$\ddot{y} + C_5 \frac{\mu_l}{\rho_l d_d^2} \dot{y} + C_4 \frac{\sigma}{\rho_l d_d^3} y = \frac{C_3 \rho_g u_{rel}^2}{C_6 \rho_l d_d} \ , \tag{5.27}$$

which can be solved as

$$y(t) = \frac{C_3}{C_4 C_6} We_d + e^{-t/t_d}((y(0) - \frac{C_3}{C_4 C_6} We_d) cos(\Omega t) + \frac{1}{\Omega}(\dot{y}(0) + \frac{y(0) - \frac{C_3}{C_4 C_6} We_d}{t_d}) sin(\Omega t)) \ , \tag{5.28}$$

where

$$\frac{1}{t_d} = C_5 \frac{\mu_l}{2\rho_l d_d^2}, \tag{5.29}$$

$$\Omega = C_4 \frac{\sigma}{\rho_l d_d^3} - \frac{1}{t_d^2} \ . \tag{5.30}$$

The constants, applied according to [83], are set to

$$C_3 = \frac{5}{12} \ , \qquad C_4 = 1 \ , \qquad C_5 = \frac{10}{4} \qquad \text{and} \qquad C_6 = \frac{1}{4} \ . \tag{5.31}$$

If the droplet distortion parameter exceeds unity, the droplet breaks up into new droplets of $We_d = 12$. The number of the newly created droplet follows from Eq. (5.21).

5.2.3 Droplet Evaporation

Evaporation is taken into account by an evaporation model, which assumes that the droplet is composed of a single-component liquid and has a spherical shape with uniform properties as described in [87]. The energy balance for a single particle, neglecting the kinetic energy related to the mass leaving the droplet is given by

$$m_d c_{p,l} \frac{dT_d}{dt} = \dot{Q} + \dot{m}_d h_L, \tag{5.32}$$

where $c_{p,l}$ is the specific heat of the liquid and h_L the latent heat. The left hand side of the equation is the total energy change of the droplet due to evaporation, the first term on the right hand side represents the

convective and conductive heat transfer and the last term the latent heat of vaporization. The heat transfer can be obtained from a form of the Fourier law of heat conduction,

$$Q = \frac{D_{th}(T_g - T_d)}{d_d} Nu, \tag{5.33}$$

which indicates that the rate of heat transfer is proportional to the temperature gradient. The Nusselt number, Nu, is defined as the ratio of the convective heat transfer at the droplet surface and the conductive heat transfer in the gas,

$$Nu = \frac{h_{th} L}{\zeta} . \tag{5.34}$$

The thermal conductivity is denoted by ζ and is defined as the product of the molecular thermal diffusivity, D_{th}, and the heat capacity, $\rho_l c_{p,l}$. L is a characteristic length and equals in the case of a droplet the droplet diameter. It can be derived for drops from the Ranz-Marshall correlation [88] according to

$$Nu = 2 + 0.6\sqrt{Re_d}\sqrt[3]{Pr} . \tag{5.35}$$

The Prandtl number, Pr, is defined as the ratio of molecular momentum to heat diffusion,

$$Pr = \nu_g / D_{th}. \tag{5.36}$$

The last term in the expression for Nu reflects the increase of heat transfer due to free and forced convection.

The change of mass in the term for the latent heat of vaporization in Eq. (5.32) is obtained from the change of the droplet diameter due to evaporation, which is given by the Frössling equation as:

$$\frac{dd_d}{dt} = -\frac{2\rho_g D_m}{\rho_l d_d} \frac{Y_{l,s} - Y_{l,\infty}}{1 - Y_{l,s}} Sh \tag{5.37}$$

The liquid vapour mass fraction at the surface is denoted as $Y_{l,s}$, the liquid vapour mass fraction in the free stream as $Y_{l,\infty}$. The Sherwood

number, Sh, is defined as the ratio of the convective mass transfer at the droplet surface and the diffusive mass transfer in the gas,

$$Sh \;=\; \frac{h_m L}{D_m} \;. \tag{5.38}$$

It can be derived for drops from the Ranz-Marshall correlation [88] according to

$$Sh \;=\; 2 + 0.6\sqrt{Re_d}\sqrt[3]{Sc} \;. \tag{5.39}$$

The Schmidt number, Sc, is defined as the ratio of molecular momentum to mass diffusion,

$$Sc \;=\; \nu_g / D_m \;. \tag{5.40}$$

Similar to the expression for Nu, the last term in the correlation for Sh accounts for free and forced convection effects.

With these definitions, Eq. (5.33) can be solved for the new droplet diameter.

CHAPTER 6

NUMERICS

6.1 Discretization Schemes

6.1.1 The Volume of Fluid Approach

The governing equations are discretized by the Finite Difference Method (FDM). The convective terms are approximated by a third-order upwind scheme (Eq. (6.1)), given by [89]. The pressure terms (Eq. (6.2)) and the diffusive terms (Eq. (6.3)) are approximated by a fourth-order scheme and the time derivatives are approximated by an implicit second-order upwind scheme (Eq. (6.4)).

$$\left(u\frac{\partial\phi}{\partial x}\right)_j = \frac{u_j(\phi_{j-2} - 8(\phi_{j-1} - \phi_{j+1}) - \phi_{j+2})}{12h} + \frac{|u_j|(\phi_{j+2} - 4(\phi_{j-2} + \phi_{j-1} + \phi_{j+1}) + 6\phi_j)}{12h} + O(h^3) \quad (6.1)$$

$$\left(\frac{\partial\phi}{\partial x}\right)_j = \frac{\phi_{j-1} - 27(\phi_j - \phi_{j+1}) - \phi_{j+2}}{24h} + O(h^4) \quad (6.2)$$

$$\left(\frac{\partial^2\phi}{\partial x^2}\right)_j = \frac{-\phi_{j-2} + 16\phi_{j-1} - 30\phi_j + 16\phi_{j+1} - \phi_{j+2}}{12h^2} + O(h^4) \quad (6.3)$$

$$\left(\frac{\partial\phi}{\partial t}\right)_j^t = \frac{3\phi_j^t - 4\phi_j^{t-1} + \phi_j^{t-2}}{2\Delta t} + O(\Delta t^2) \quad (6.4)$$

For grid points close to the boundary of the domain lower order approximations are used.

6.1.2 The Lagrangian Particle Tracking Approach

The governing equations are discretized by the FDM scheme. The convective terms are approximated by an up to fifth-order Weighted Essentially Non Oscillatory (WENO) scheme [90]. The scheme applies three approximations which use three different computational stencils and combines them with weighting factors depending on the flow situation. Thus, it is possible to handle discontinuities in the flow field, e.g. at shock waves or flame fronts. The smoothness of the three approximations is evaluated and the highest weight is applied to the smoothest approximation, while a weight close to zero is applied to approximations that show discontinuities. The efficiency of the WENO scheme has been shown in [82] for a one-dimensional step. The derivatives are computed from the fluxes at half-distance to the neighbouring cells:

$$\left(\frac{\partial\phi}{\partial x}\right)_j = \frac{1}{h}(\hat{\phi}_{j+1/2} - \hat{\phi}_{j-1/2}) \quad (6.5)$$

The fluxes are derived from a combination of three approximations, weighted with w_k as

$$\hat{\phi}_{j+1/2} = w_1\hat{\phi}^{(1)}_{j+1/2} + w_2\hat{\phi}^{(2)}_{j+1/2} + w_3\hat{\phi}^{(3)}_{j+1/2}\ , \quad (6.6)$$

where the three approximations on three different stencils are given by

$$\hat{\phi}^{(1)}_{j+1/2} = \frac{1}{3}\phi_{j-2} - \frac{7}{6}\phi_{j-1} + \frac{11}{6}\phi_j \tag{6.7}$$

$$\hat{\phi}^{(2)}_{j+1/2} = -\frac{1}{6}\phi_{j-1} + \frac{5}{6}\phi_j + \frac{1}{3}\phi_{j+1} \tag{6.8}$$

$$\hat{\phi}^{(3)}_{j+1/2} = \frac{1}{3}\phi_j + \frac{5}{6}\phi_{j+1} - \frac{1}{6}\phi_{j+2} \tag{6.9}$$

and the weighting factors by

$$w_k = \frac{\Omega_k}{\Omega_1 + \Omega_2 + \Omega_3} \ . \tag{6.10}$$

Ω_k is defined as

$$\Omega_k = \frac{\gamma_k}{(\epsilon + \beta_k)2} \ , \tag{6.11}$$

where γ_k are the linear weights

$$\gamma_1 = \frac{1}{10} \quad \gamma_2 = \frac{6}{10} \quad \text{and} \quad \gamma_3 = \frac{3}{10} \tag{6.12}$$

and β_k are the smoothness indicators for each stencil given by

$$\beta_1 = \frac{13}{12}(\phi_{j-2} - 2\phi_{j-1} + \phi_j)^2 + \frac{1}{4}(\phi_{j-2} - 4\phi_{j-1} + 3\phi_j)^2 \tag{6.13}$$

$$\beta_2 = \frac{13}{12}(\phi_{j-1} - 2\phi_j + \phi_{j+1})^2 + \frac{1}{4}(\phi_{j-1} - \phi_{j+1})^2 \tag{6.14}$$

$$\beta_3 = \frac{13}{12}(\phi_j - 2\phi_{j+1} + \phi_{j+2})^2 + \frac{1}{4}(3\phi_j - 4\phi_{j+1} + \phi_{j+2})^2 \tag{6.15}$$

In a smooth region the three stencils are combined with the same weight, which leads to fifth-order accuracy.

The pressure terms (Eq. (6.2)) and the diffusive terms (Eq. (6.3)) are approximated by a fourth-order scheme and the time derivatives are approximated by an implicit second-order upwind scheme (Eq. (6.4)). For grid points close to the boundary of the domain, lower order approximations are used.

6.2 Solver

The governing equations are solved applying the Semi-Implicit Method for Pressure Linked Equations (SIMPLE) algorithm, according to [91] and [92], which follows the following steps in each time-step:

1. The pressure field is guessed from the previous time-step.
2. The momentum equations are updated for the time-step to obtain the velocity field using the guessed pressure field.
3. The pressure and velocity fields are corrected to satisfy continuity.
4. Step 2 and 3 are repeated until the solution converges.

In step 2, the system of equations is solved using a multigrid method that employs the Gauss-Seidel relaxation scheme. Furthermore, to increase computational efficiency, the single step defect correction method is used, which has been proven to be accurate in [93], where the convergence of a single/few step defect correction scheme is shown.

6.3 Numerical Accuracy

Numerical solutions of the flow of fluids are only approximated solutions. Besides the errors that are introduced by estimated initial conditions, boundary conditions or bugs in the code, numerical solutions suffer from three systematic errors:

- Model error
- Iteration error
- Discretization error

The model error is defined as the difference between the mathematical model of the flow (the governing equations and the applied models) and the real flow and is discussed in Ch. 3 - 5. The iteration error is defined as the difference between the exact and the iterative solution of the algebraic difference equations. In this work iterative convergence is achieved

by ensuring that the residuals are sufficiently small in each time-step. The discretization error is defined as the difference between the exact solutions of the governing equations and the exact solution of the algebraic difference equations. It corresponds to the truncation error of the discretization schemes and is considered in the following.

The error introduced in the numerical solution due to discretization is estimated by the procedure given in [94], which applies the method of the Richardson-extrapolation [95]: If at least three solutions of the same flow are available on three different grid resolutions, the numerical error on the finest grid can be derived. This is quite exact as long as the convergence of the solution is monotone with increasing resolution. If the used computational grids are rectangular and equidistant, and the grids are refined by the factor 2, than the apparent order, χ, of the numerical method can be derived as

$$\chi \;=\; \frac{\ln(\frac{\phi_2-\phi_3}{\phi_1-\phi_2})}{\ln 2} \;. \tag{6.16}$$

ϕ is a relevant variable contained in the solution, the indices correspond to the grid resolutions, where

$$h_3 \;=\; 2 \cdot h_2 \;=\; 4 \cdot h_1 \;. \tag{6.17}$$

From this, the numerical uncertainty on the finest grid can be estimated as

$$\psi_1 \;\approx\; 1.25 \;\cdot\; \frac{\phi_1 - \phi_2}{2^p - 1} \;, \tag{6.18}$$

which gives the relative uncertainty when normalised to the finest grid solution

$$\psi_1^* \;=\; \psi_1 \;/\; \phi_1 \;. \tag{6.19}$$

VOF

A case of a liquid jet injected into still gas is simulated on three different grid resolutions to estimate the discretization error of the VOF approach. The liquid jet inlet has a diameter of $d_{inj} = 10^{-4}m$ and the injection

	$\langle u_{str} \rangle$		
	y=0.0	y=0.5	y=1.0
h_1	0.05	0.05	0.05
h_2	0.1	0.1	0.1
h_3	0.2	0.2	0.2
ϕ_1	0.812	0.707	0.466
ϕ_2	0.827	0.689	0.415
ϕ_3	0.975	0.454	0.133
χ	3.3	3.7	2.5
ψ_1^*	0.2 %	0.4 %	10.6 %

Table 6.1: Error estimates of the VOF results. Derived for the average streamwise velocity at points located at $z = 27.5$ and $x = 0$.

speed is a top hat profile of $U_{inj} = 500m/s$. The results are normalised to d_{inj} and U_{inj}. The liquid-gas density ratio is $\frac{\rho_l}{\rho_g} = 10$, the liquid-gas viscosity ratio is $\frac{\mu_l}{\mu_g} = 3.42$, the jet Reynolds number is $Re_{jet} = 15000$ and the jet Weber number is $We_{jet} = 10000$. The domain is of the size $8 \cdot 8 \cdot 31\ d_{noz}$. As variable ϕ, the average streamwise velocity of three points has been chosen. The location of the points and the results are given in Tab. 6.1

The apparent order of discretization is between 2.5 and 3.7, which is in the expected range. The relative errors are considered to be sufficiently low. It has to be noted that for all grids there is no grid point exactly located at the above mentioned coordinates, but the values for ϕ are interpolated in an appropriate manner from the neighbouring grid points, introducing interpolation errors.

LPT

Grid dependency is an inherent problem for simulations in LPT framework. On one hand one wishes the grid to be fine to reduce the discretization error. On the other hand the cells have to be large enough so that the droplets are so small that the volume it displaces is negligible (see Ch. 5). Thus, one cannot expect the results to converge for finer

grids and results on finer grids are not necessarily more accurate.

However, simplified cases are run with the LPT approach to analyse its behaviour for grid refinements. The injection nozzle has a diameter of 150 μm. The domain is a cuboid of the side lengths $33 \cdot 33 \cdot 66\, d_{noz}$. As a liquid, decane is injected with a velocity of 150 m/s. The droplet diameters follow at injection a Rosin-Rammler distribution. The SMD of the droplets at the injection nozzle is 5 μm. As variable ϕ the average streamwise velocity (normalised to the injection velocity) and the average droplet diameter of two points has been chosen. The location of the points and the results are given in Tab. 6.2

	$\langle u_{str} \rangle$		$\langle d_d \rangle$	
	y=11.6	y=15	y=5	y=11.6
h_1	1.0	1.0	1.0	1.0
h_2	2.0	2.0	2.0	2.0
h_3	4.0	4.0	4.0	4.0
ϕ_1	0.011	0.243	0.0 μm	0.81 μm
ϕ_2	0.013	0.261	0.96 μm	11.2 μm
ϕ_3	0.067	0.213	0.88 μm	9.2 μm
χ	1.25	1.44	3.61	2.04
ψ_1^*	30.7 %	6.2 %	12.1 %	35.1 %

Table 6.2: Error estimates of the LPT results. Derived for the average streamwise velocity and the average droplet diameter at points located at $z = 55$ and $x = 0$.

CHAPTER 7

COUPLING VOF TO LPT

The underlying physical assumptions of the VOF method are adequate to simulate a spray in all regimes. Other than the surface tension and the SGS terms, in the case of an LES simulation, this approach is model free. The drawback of such an interface resolving approach is that, as every droplet needs to be resolved by the computational grid, the required spatial resolution and, therefore, the computational costs are very high. Especially in the dilute spray regime, where there is a huge number of small droplets present, the required resolution is so high that the method is no longer practical.

The LPT approach on the other hand reflects the underlying physics to a lower degree but is computationally more efficient. The basic assumptions include that the droplets are spherical and do not displace ambient fluid. In other words, the computational cell is assumed to be much larger than the volume of the droplets it contains. Thus, contrary to the VOF method, the droplets are not resolved on the computational grid, but are tracked individually in a Lagrangian framework. Therefore, models need to be introduced for all droplet related processes, such as the primary breakup of the liquid jet, droplet secondary breakup, droplet evaporation, aerodynamic interaction with the surrounding gas, droplet-droplet collisions, coalescence or interactions with neighbouring

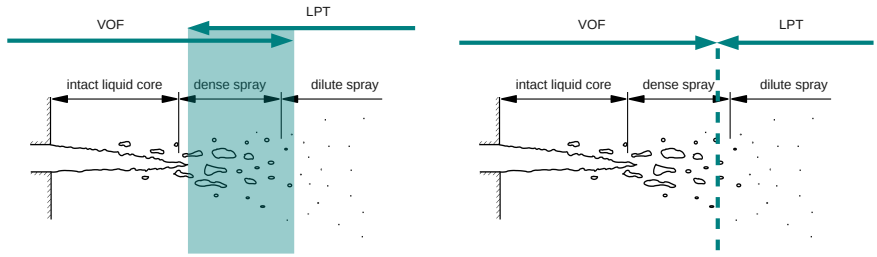

(a) DCA. (b) SCA.

Figure 7.1: Schemes of VOF-LPT coupling approaches.

solid walls. Numerical models to describe these processes are usually empirical models based on experimental results and are only valid in certain ranges. This reduces the physical applicability mainly in the intact liquid core and dense spray regime, where primary breakup occurs and droplet-droplet interaction are the most frequent. There, liquid structures are mostly non-spherical, which reduces the applicability of droplet breakup and evaporation models. An assumed diameter distribution, usually a Rossin-Rammler distribution, is used as an initial condition instead of obtaining droplet diameters resulting from a simulation. However, the underlying physics are well reflected in the dilute spray regime. Due to upstream breakups, the droplets are small and the liquid surface tension tends to give them a spherical shape. Due to the high spacing, droplet-droplet interactions are rare. Small spherical droplets support the applicability of droplet models, which are often developed for spherical, isolated droplets.

Due to the above considerations, coupling methods have been developed: the intact liquid core and the dense spray regime are simulated using an interface capturing method method, the dilute spray regime is calculated using the LPT method and both are linked by a coupling method. The Direct Coupling Approach (DCA), depicted schematically in Fig. 7.1(a), has been chosen in [24] and [25]. Here the physical domain of the VOF/level-set and the LPT simulation are overlapping, which makes it possible to decide for each individual liquid structure by which method it is more appropriately described. Compared to a full VOF sim-

ulation, the physical applicability is only slightly reduced by this coupling approach, as a droplet is only tracked in the LPT frame if it is judged to be within the validity range of the used droplet models. Further downstream the spray is assumed to be even more dilute and the droplets are spherical, so that the whole spray is described by the LPT method. Compared to the total size of the domain, this downstream point is close to the injection nozzle, therefore the physical size of the VOF domain is significantly smaller than the one of the LPT domain. This in turn leads to a significantly better computational efficiency, as compared to the pure VOF method.

The drawback of the above-described coupling method is that, due to the fact that the cell size and the timescales on the VOF part of the simulation are much smaller than the ones of the LPT simulation, the ratio of the computational time to the propagation distance of a droplet is much larger for the VOF than for the LPT simulation. Thus, for the simulation of a usual gas turbine or a Diesel injection, the LPT simulation has to 'wait' for inputs from the VOF simulation. To overcome this drawback, a Statistical Coupling Approach (SCA), see Fig. 7.1(b), has been developed here. The intact liquid core and dense spray regime are simulated using the VOF method. A fixed plane in the domain is determined for which the LPT method is applicable for most of the droplets. At this plane statistical data of the droplet distribution and the gaseous phase are extracted. When convergence is reached in the results, these statistics are used as initial conditions for the LPT simulation. Through this, the LPT simulation does not have to wait for the VOF simulation any longer, which increases the computational efficiency compared to the above described straightforward approach significantly. An advantage of this approach is that the primary breakup of the spray is simulated once and the statistical results can be used to start several LPT simulations, e.g. for different domain sizes. Another advantage is that the results from one VOF simulation can also be used to start a LPT simulation containing several injection nozzles. The drawback of this approach is that the plane to couple VOF and LPT is fixed. It is located at an appropriate position only for most, but not for all droplets. The fact that the switch from VOF to LPT is not decided on an individual droplet level, reduces the physical applicability of this method, while it is still

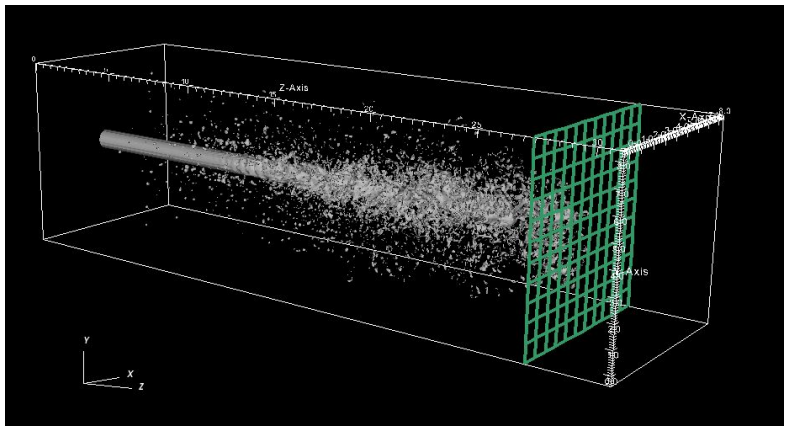

Figure 7.2: Location of the Coupling Layer (CL).

higher than a pure LPT approach. Also, the assumption has to be made that there are no upstream back coupling effects from the LPT to the VOF simulation.

7.1 The Statistical Coupling Approach (SCA)

The methodology of the SCA is described in the papers II, IV, V and X and summarised below.

Primary breakup creates a large number of droplets of different scales and shapes. A layer, called the Coupling Layer (CL) is introduced close to the outlet where the liquid droplets pass through. Statistical data is generated in this layer where the spray is nearly dilute. The CL is considered to be far enough downstream from the injector that the spray is dilute enough to comply with the assumptions of the LPT approach. The location of the CL is schematically shown as a green grid in Fig. 7.2.

An algorithm has been developed to identify the surface area of the liquid structure that passes the CL at a time instance. This algorithm is based on the one described in [96] and is extended to time dependent problems. The irregular liquid structures are identified and an equivalent radius of a spherical droplet, as well as its center of gravity and droplet

velocity vector is calculated. Test cases have been run in Paper II on different grid resolutions to test the accuracy of the extraction method applied at the coupling layer. It has been shown that, if the droplet diameter is resolved by at least 3 cells ($d_d/h > 3$), then the results are considered to be sufficiently accurate. For this resolution the test cases show an error of a maximum of 30% and a minimum of 10% in the identified droplet volume.

As the timescales of the VOF simulation are much smaller than the ones required for the LPT simulation, it is not practical to synchronise both calculations and to inject each droplet that has been extracted in the VOF simulation into the LPT simulation. Instead, on the VOF side statistical data is extracted and used to perform a Monte-Carlo simulation on the LPT side. When a droplet is injected on the LPT side, the droplet diameter, the droplet velocity vector and the droplet position vector must be given. Rotational symmetry is assumed and the streamwise position is defined by the location of the coupling layer, thus, the number of needed parameters reduces to four: the droplet diameter d_d, streamwise velocity u_{str}, spanwise velocity u_{spa} and spanwise position $\vec{r}$. The droplet temperature and density are fixed, as the spray is assumed to be isothermal and incompressible on the VOF side. If there exists a statistical dependence between two or more of these parameters, this information is not lost in the coupling procedure. For those of the above variables that cannot be determined by correlations to other parameters, independent Monte-Carlo simulations will be performed. The method developed to perform the Monte-Carlo simulations is based on [87].

The coupling layer is also used to link the gaseous phase of the VOF to the LPT simulation. As the time and length scales of the continuous phase in the LPT simulation are of an order larger than in the VOF simulation, there will be some interpolation in space and time to be done when applying the field to the LPT simulation. The fluctuations of the small scale structures will be filtered out during the coupling of both simulations. Therefore the average velocities are used as a steady gas inlet condition in the LPT simulation.

CHAPTER 8

SET-UP AND RESULTS

8.1 Volume of Fluid Simulations

The results of the VOF simulations are published and attached as papers II, III and IX. They are summarised shortly in this section.

Simulation Set-up

The set-up of the domain and the arrangement of the boundaries are shown in Fig. 8.1.

As boundary condition at the inlet, the Dirichlet condition is applied, i.e. fixed values are given, and at the outlet zero-gradient condition is applied to the velocity components and scalars. At the walls the no-slip condition is applied for the velocity components and the zero-gradient condition is applied to the scalars. The diameter of the injection nozzle is $d_{noz} = 100\,\mu m$; the following results are normalised with this value. The domain is of the size $8 \cdot 8 \cdot 31\, d_{noz}$. According to the findings in Paper IX, this is large enough so that the jet is not significantly influenced by the wall boundary conditions and that the jet will completely break up in the domain. Following Ch. 6.3, the computational cells are of a size of $h = 0.05\, d_{noz}$. The CL is located at the downstream position $z = 30\, d_{noz}$.

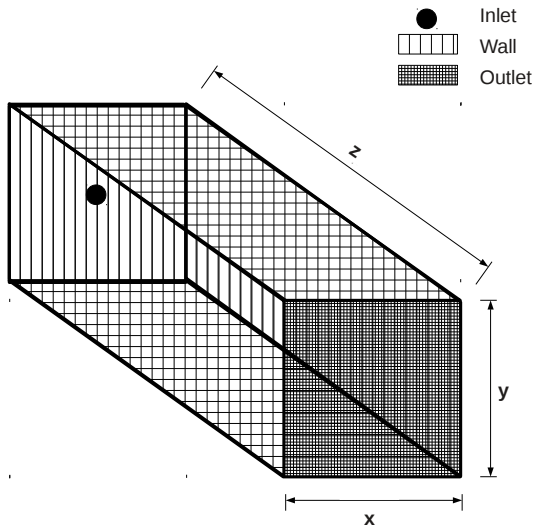

Figure 8.1: Domain of the VOF simulation.

The behaviour of the breakup of the jet is analysed depending on variations in the liquid properties. The parameters of the simulated cases are shown in Tab. 8.1.

CASE	$\mathrm{Re}_{\mathrm{jet}}$	$\frac{\rho_\mathrm{l}}{\rho_\mathrm{g}}$	$\frac{\mu_\mathrm{l}}{\mu_\mathrm{g}}$	$\mathrm{We}_{\mathrm{jet}}$
A	14964	41.4	3.419	10000
B	14964	41.4	3.419	100000
C	14964	10	3.419	10000
D	14964	20	3.419	10000
E	14964	30	3.419	10000
F	14964	30	1	10000
G	14964	30	2	10000
H	14964	30	7	10000

Table 8.1: Fluid properties used in VOF computations.

Results

A snapshot of the penetration of the liquid jet of case C is shown in Fig. 8.2(a). Fig. 8.2(b) shows the jet very short after the beginning of the injection. The head of the jet forms a shape like a mushroom cap, which is typical for the Rayleigh-Taylor instability. In Fig. 8.2(c) a detail of the jet at at later stage is enlarged. One can see the formation of Kelvin-Helmholtz instabilities at the surface. These lead to the stripping off of small droplets from the jet surface. As these droplets are small, their Stokes number is also small, hence their trajectories are strongly influenced by turbulent eddies, which leads to the dispersion of the spray.

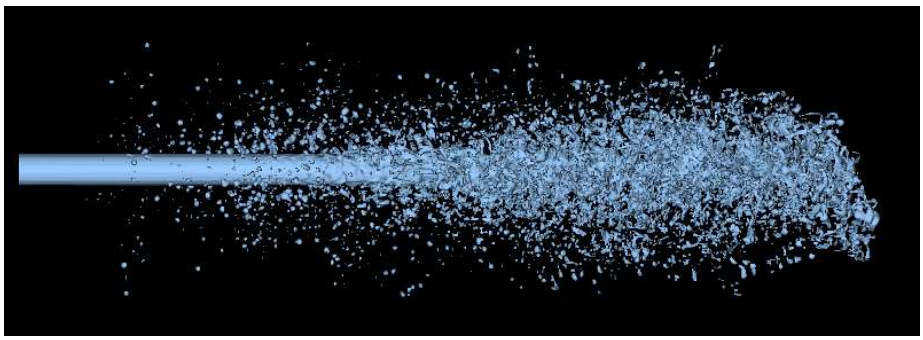

(a) The complete jet at $t = 42.6$. The blue surface describes the isosurface of $\alpha = 0.5$.

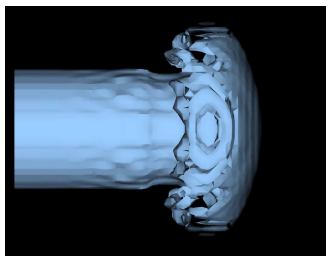

(b) The jet at $t = 1.1$, forming a typical mushroom cap.

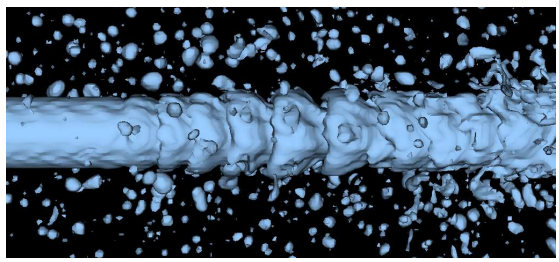

(c) Detail of the jet between $z = 8$ and $z = 16$ at $t = 58.6$, forming Kelvin-Helmholtz instabilities on the liquid surface.

Figure 8.2: Snapshots of the jet penetration of case C.

In Fig. 8.3 the droplet diameter distribution, extracted at the Coupling Layer (CL), is shown for varying liquid-gas density and viscosity ratios. It is interesting to note that the distributions for all the simulations show two peaks: one for very small droplet diameter and one around $d_d \approx 0.08$. These seem to be related to two breakup mechanisms concurrently dominant, as already noted in Fig. 8.2(b) and 8.2(c): one mechanism which strips off small droplets from the surface and which is assumed to be related to Kelvin-Helmholtz instabilities and one mechanism which creates larger liquid structures and is assumed to be related to Rayleigh-Taylor instabilities. Such two peak distributions have also been found experimentally in [97].

Fig. 8.3(a) shows that the amount of small droplets at the first peak is the larger, the smaller the liquid-gas density ratio is. For smaller liquid-gas density ratios the kinetic energy of the gas is larger and it will consequently strip off more small droplets. It can be seen in Fig. 8.3(b)

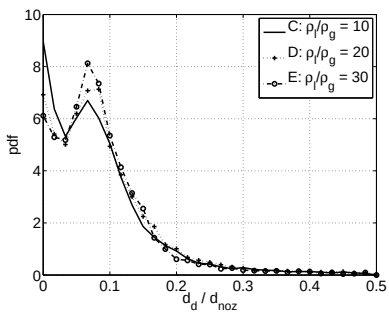

(a) Droplet diameter distribution for variations in the density ratio.

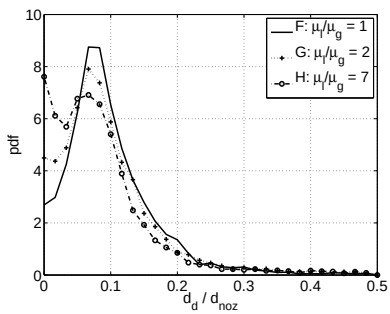

(b) Droplet diameter distribution for variations in the viscosity ratio.

Figure 8.3: Droplet distributions resulting from the VOF simulations.

that increasing the liquid-gas viscosity ratio from 1 to 2 and from 2 to 7 leads to smaller droplets. As the jet Reynolds number is kept constant, an increase in the liquid-gas viscosity ratio means in fact a decrease in the gas viscosity. This results in an increased Reynolds number in the gas flow and hence more turbulent structures. The increase of turbulent structures in the gas phase enhances the instability mechanisms of the liquid surface and therefore leads to a faster breakup and thereby to

smaller droplets. The drawn conclusions concerning the stabilising and destabilising effects of the fluid properties are valid in the range that is under investigation. For example for jets of lower We numbers, one can as well observe the destabilising effects of surface tension and viscosity [98–100].

8.2 Lagrangian Particle Tracking Simulations

The results of the LPT simulations are attached as paper I and are summarised in this section.

Simulation Set-up

The injection of liquid fuel into a gas turbine combustor (shown in Fig. 8.4) is simulated using the LPT framework. To give a detailed view on the turbulent structure of the fuel spray, several monitoring points are introduced in the domain. The spray structure is monitored at 154 monitoring points at 5 axial positions. At these monitoring points the droplet diameter distribution is analysed. The dimensions of the domain and the location of the monitoring points are shown in Fig. 8.5. The diameter of the injection nozzle is $d_{noz} = 500\,\mu m$; the following results are normalised with this value. The length of the domain in streamwise direction is $230\,d_{noz}$, the maximum size in spanwise direction is $44\,d_{noz}$.

The structure of the spray depending on variations in the fuel properties is analysed to evaluate the fuel flexibility of gas turbines. The chosen properties are summarised in Tab. 8.2.

The liquid is assumed to be injected as dispersed droplets and, thus, no atomization model for the initial breakup is used. The droplet diameters at injection satisfy a Rosin-Rammler distribution. The SMD of the droplets at the injection nozzle is $60\,\mu m$.

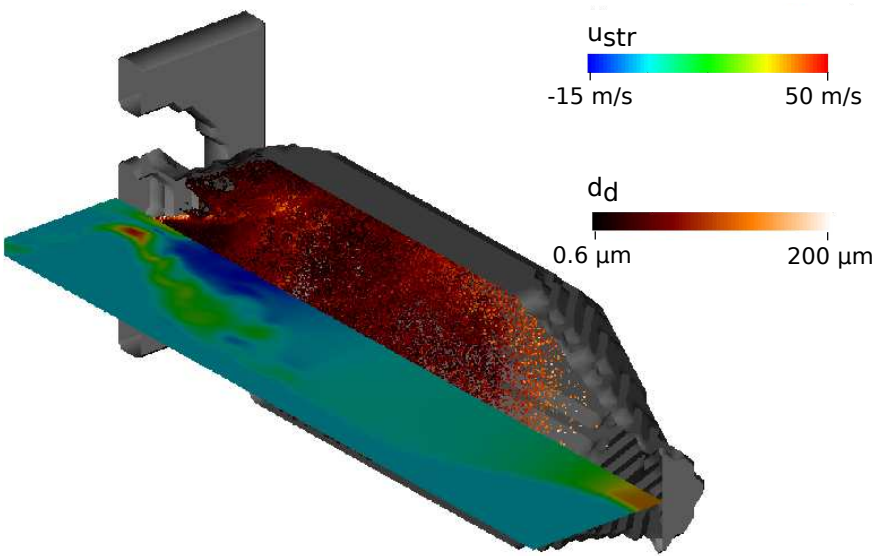

Figure 8.4: Snapshot of the droplet distribution, the streamwise velocity of the gas and the geometry of the burner.

CASE	σ	ν_l	ρ_l
1	0.01	$2.85 \cdot 10^{-6}$	700
2	0.02	$2.85 \cdot 10^{-6}$	700
3	0.04	$2.85 \cdot 10^{-6}$	700
4	0.08	$2.85 \cdot 10^{-6}$	700
5	0.02	$1.00 \cdot 10^{-6}$	700
6	0.02	$1.00 \cdot 10^{-5}$	700
7	0.02	$1.00 \cdot 10^{-4}$	700
8	0.02	$1.00 \cdot 10^{-3}$	700
9	0.02	$2.85 \cdot 10^{-6}$	200
10	0.02	$2.85 \cdot 10^{-6}$	400
11	0.02	$2.85 \cdot 10^{-6}$	800
12	0.02	$2.85 \cdot 10^{-6}$	1600

Table 8.2: Summary of fuel properties used in LPT computations.

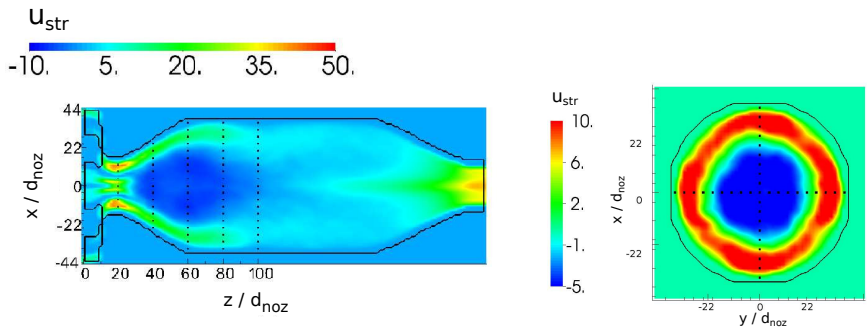

(a) Cut at $y = 0$. (b) Cut at $z = 60\, d_{noz}$.

Figure 8.5: Average streamwise velocity of the gas for case 1, geometry of the burner and monitoring points.

Results

Typical results of the pdfs are shown in Figs. 8.6(a) and 8.6(c). In both monitoring points considered in the figure, the stabilising effect of surface tension on the droplets can be seen. For smaller surface tensions the droplets breakup is faster while the pdfs for simulations with larger surface tension show larger droplets. It can also be observed that in Fig. 8.6(c), which is for a monitoring point of a larger radial distance to the centreline than the left figure, the droplets for all simulations are smaller. This can be explained by the Stokes number dependency of the spray (Fig. 2.4). Smaller droplets tend to be transported outside of the spray by the large vortices created by the spray, while larger droplets tend to be less affected. Sample results for the effects of variation of fuel viscosity are shown in Fig. 8.6(b) and Fig. 8.6(d). The viscosity yields a similar effect as the surface tension: it acts against the deformation of the droplet and therefore it has a stabilising effect. Thus, the smaller the liquid viscosity the more bag breakup that occurs and the smaller the droplets.

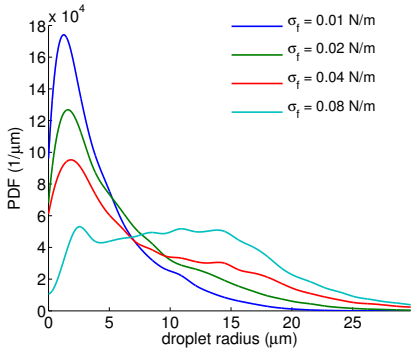

(a) Droplet radius pdf at $x = 16\, d_{noz}, y = 0, z = 40\, d_{noz}$.

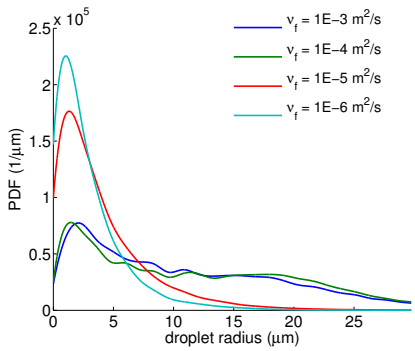

(b) Droplet radius pdf at $x = 20\, d_{noz}, y = 0, z = 40\, d_{noz}$.

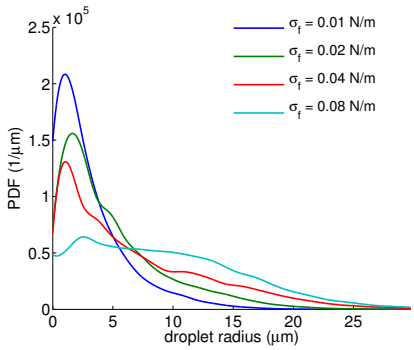

(c) Droplet radius pdf at $x = 20\, d_{noz}, y = 0, z = 40\, d_{noz}$.

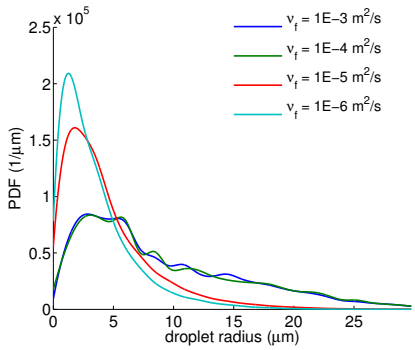

(d) Droplet radius pdf at $x = 24\, d_{noz}, y = 0, z = 40\, d_{noz}$.

Figure 8.6: Droplet distributions in the LPT simulations.

8.3 VOF-LPT Coupling

The results of the VOF-LPT coupling simulations are attached as papers IV, V and X. They are summarised in this section.

Simulation Set-up

A test case of a liquid spray is simulated applying the SCA described in Ch. 7.

The injection speed u_{inj} of the simulated spray is $500 m/s$ of a top hat profile, the nozzle diameter d_{noz} is 10^{-4} m, the results are normalised to these values. The jet Reynolds number Re_{jet} equals 15000, the jet Weber number We_{jet} is $1.2 \cdot 10^6$, the liquid-gas density ratio is 10 and the liquid-gas viscosity ratio is 46. The ambient gas density is $14.8 kg/m^3$, the ambient gas temperature is $1150\,K$.

To define an appropriate position for the CL, a VOF simulation with a domain of the size of $8 \cdot 8 \cdot 42\, d_{noz}$ is run. $z = 29.6$ is chosen to be the location of the CL, as here the average liquid volume fraction is lower than 0.25 at the centreline (see Fig. 8.7). This decision leads to a computational domain for the coupling case as schematically shown in Fig. 8.8. The domain used for the VOF simulation is of the size of $8 \cdot 8 \cdot 29.6\, d_{noz}$. A Cartesian equidistant grid of the cell size $h = 0.05\, d_{noz}$ is used. This results in $15 \cdot 10^6$ grid points. The VOF domain is followed by the LPT domain, which is of a size of $30 \cdot 30 \cdot 11\, d_{noz}$. A Cartesian equidistant grid of the cell size $h = 0.25\, d_{noz}$ is used. This results in $6.3 \cdot 10^5$ grid points.

For assessing the developed SCA, a simulation for the same case but applying the DCA is simulated. As for the SCA, no overlapping of the domains was used for the DCA. Thus, both simulations use the identical simulation in the VOF domain. The physical simulation time of the VOF simulation corresponds approximately to the time the jet requires to cross the domain 15 times.

Results

The droplet diameter, streamwise velocity, the spanwise velocity and the spanwise position are extracted from the VOF simulation at the coupling

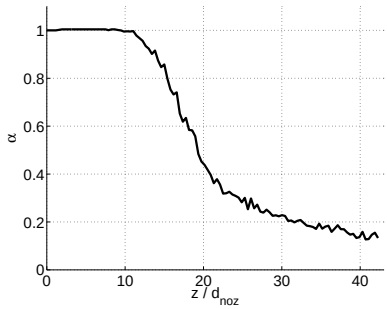

Figure 8.7: Average liquid volume fraction along the jet centreline.

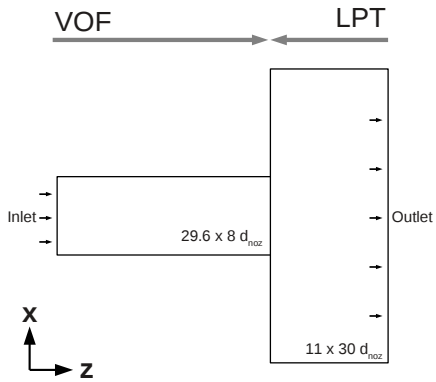

Figure 8.8: Arrangement of the computational domain. The y-dimension is identical to x-dimension.

layer. The correlation coefficients show that there is a correlation between the streamwise velocity and the spanwise position of the droplets, while all combinations of other parameters show only a minor correlation. Following this finding, for the SCA, three independent Monte-Carlo simulations are performed for the droplet radius, the streamwise velocity and the spanwise velocity. The spanwise position, r_{spa}, is determined by a relationship from the streamwise velocity, u_{str}. For this case the relationship is

$$|r_{spa}| = max(0, -5 \cdot u_{str} + 4) \ . \tag{8.1}$$

The droplet diameter distribution resulting from the VOF simulation is shown in Fig. 8.9(a). It can be noted that besides a large number of very small droplets, a peak in the distribution at around $d_d = 0.08$ is produced. This is usually not covered by starting a LPT simulation from a standard distribution, e.g. a Rosin-Rammler distribution. The distribution of streamwise velocities is given in Fig. 8.9(b), the distribution of spanwise velocities in Fig. 8.9(c). The LPT simulation using the SCA is started with these statistical distributions, by performing Monte-Carlo simulations. The results of these Monte-Carlo simulations

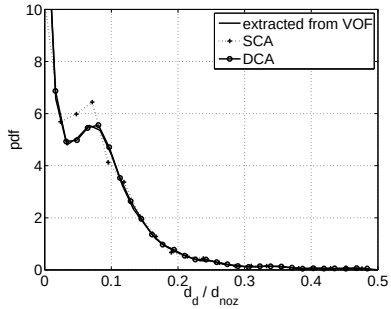

(a) Droplet diameter distribution.

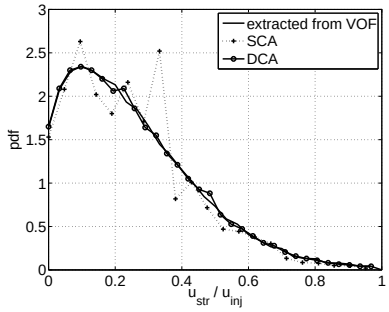

(b) Streamwise velocity distribution.

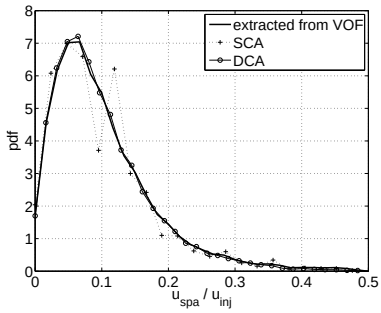

(c) Spanwise velocity distribution.

Figure 8.9: Droplet distributions extracted from the VOF and injected in the LPT simulations applying the SCA and DCA.

are shown as well in Fig. 8.9(a) to Fig. 8.9(c). The distributions resulting from the Monte-Carlo simulations converge to the distributions from the VOF simulation, which demonstrates the accuracy of the developed statistical coupling algorithm. The distributions of the droplets injected with the DCA approach are shown in the same figures and show as well to converge with the distributions from the VOF simulation.

A snapshot at $t = 16$ of the spray simulated with the SCA is shown in Fig. 8.10. The liquid mass that is described by the VOF method is coloured blue and the droplets tracked in Lagrangian framework are coloured red. As previously mentioned, the SCA applies only a statistical relationship between the VOF and the LPT simulation. Thus, Fig. 8.10

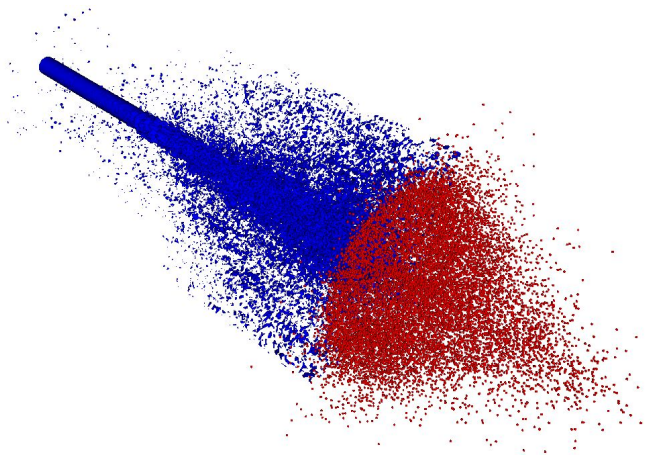

Figure 8.10: Snapshot of the simulations coupled with the SCA at t=16. Blue phase is tracked in VOF, red mass is tracked in LPT framework.

does not show one consistent realisation of the spray, but one realisation in the VOF and one realisation in the LPT domain.

The average streamwise velocity profiles of the LPT simulations, see Fig. 8.11, show a good agreement between the DCA and SCA. One possible reason for the discrepancies is the application of the stochastic parcel method in the SCA, which leads in general to a higher resolution of the droplet distribution function. Another possible reason is that the supply of droplets from the VOF simulation is due to finite simulation time not unlimited in the DCA. Thus, the properties of injected droplets are repeated at some point in time (which corresponds approximately to the liquid jet crossing 15 times the VOF domain), which is not necessary when applying the SCA. A difference between the two methods is the capturing of the beginning of the spray development: The DCA accounts naturally for the properties of the first droplets that reach the LPT domain, while the statistics in the SCA are not time resolved. But as Fig. 8.11 shows time averaged figures, this does not effect the results.

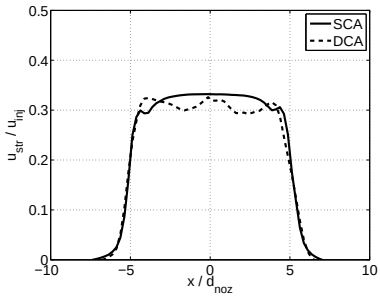

(a) Average streamwise gas velocity at $z = 28\ d_{noz}$.

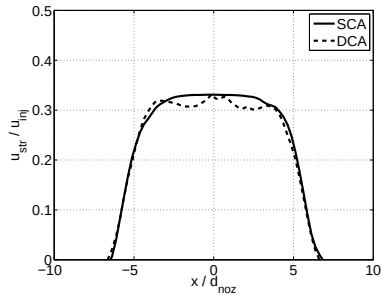

(b) Average streamwise gas velocity at $z = 30.5\ d_{noz}$.

Figure 8.11: Results of the LPT simulation, SCA compared to DCA.

Computational Efficiency

The relative computational costs for the simulated case are given in Tab. 8.3. The computational time for the VOF simulation, τ_{VOF}, is the sum of all 16 involved processors in the DCA and SCA. It is not applicable for the pure LPT approach. The SCA is significantly less expensive than the DCA, as it is only run until statistical convergence, while the DCA has to follow the generated droplets, during both, the VOF and the LPT simulations. The computational time for the LPT simulation, τ_{LPT}, is identical for all LPT simulations, with a given number of droplets, independently how the initial droplet set-up is determined. However, the LTP simulation using the DCA is larger since the stochastic parcel idea cannot be used and each droplet is tracked individually. The total computation times show that the SCA is about 4 times faster than the DCA. For a spray that is simulated until evaporation, the domain size covering the dispersed spray may be larger and, thus, more droplets are needed to be provided from the VOF simulation if the DCA is applied. Therefore, the VOF simulation has to be carried out for a longer period of time. In the SCA the VOF simulation is only done until a statistical convergence, whereby the computational time is not affected by the size of the LPT domain. For such a case the computational benefits of the SCA over the DCA are expected to be larger.

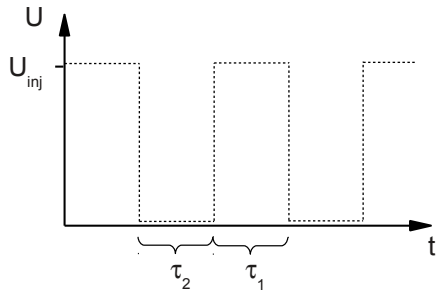

Figure 8.12: Velocity profile of pulsed liquid injection.

	τ_{VOF}	τ_{LPT}	τ_{tot}	$\frac{\tau_{\mathrm{tot}}}{\tau_{\mathrm{SCA,tot}}}$
pure LPT	–	96	96	0.0056
DCA	$6.9 \cdot 10^4$	105	$6.9 \cdot 10^4$	4.1
SCA	$1.6 \cdot 10^4$	96	$1.7 \cdot 10^4$	1

Table 8.3: Computational expenses for LPT, DCA and SCA.

8.4 Pulsed Liquid Injection

The results of the pulsed liquid injection are published and attached as paper VII and VIII. They are summarised in this section.

The aim of this study is to analyse the effect of enhanced liquid-gas mixing that is observed for jets that are injected in pulses, as described in Ch. 2.3.6.

Simulation Set-up

Liquid is injected through a nozzle with the diameter $d_{noz} = 100\,\mu m$ into quiescent air according to the velocity profile shown in Fig. 8.12. τ_1 denotes the time duration of liquid injection at a constant velocity, U_{inj}. τ_2 denotes no injection. τ_1 and τ_2 are given in non-dimensional units relating to d_{noz}/U_{inj}.

Simulations of the primary breakup of the jet are run by applying

CASE	$\mathrm{Re}_{\mathrm{jet}}$	$\frac{\rho_\mathrm{l}}{\rho_\mathrm{g}}$	$\frac{\mu_\mathrm{l}}{\mu_\mathrm{g}}$	$\mathrm{We}_{\mathrm{jet}}$	τ_1	τ_2
vof.aI	9300	1	2.8	10^8	10	10
vof.aII	9300	20	2.8	10^8	10	10
vof.bI	9300	1	2.8	10^8	10	20
vof.bII	9300	20	2.8	10^8	10	20
vof.cII	9300	20	2.8	500	10	10
vof.dII	9300	20	2.8	500	5	5
vof.eII	9300	20	2.8	500	20	20

Table 8.4: Characteristics of the VOF simulations for pulsed liquid injection.

CASE	Re_d	$\frac{\rho_\mathrm{l}}{\rho_\mathrm{g}}$	We_d	τ_1	τ_2
lpt.aI	2200	250	10	10	10
lpt.aII	2200	250	20	10	10
lpt.bI	2200	250	10	10	20
lpt.bII	2200	250	20	10	20

Table 8.5: Characteristics of the LPT simulations for pulsed liquid injection.

the VOF code and simulations of the liquid spray are run by applying the LPT method. The VOF domain is of the size $8 \cdot 8 \cdot 24\ d_{noz}$, the nozzle diameter is resolved by 18 grid cells. The flow properties of the VOF simulations are given in Tab. 8.4. The LPT domain is of the size $40 \cdot 40 \cdot 200\ d_{noz}$. Grid refinements are used, resulting in a grid that resolves the nozzle diameter with 2 grid cells. The flow properties of the LPT simulations are given in Tab. 8.5.

Results

The propagation of the jet of case vof.bI is shown in Fig. 8.13. As the Weber number is very high and the liquid density equals the gaseous density, the case is similar to a single-phase jet. In Fig. 8.13(a) the first pulse enters the domain. In Fig. 8.13(b) one can see that the pulse

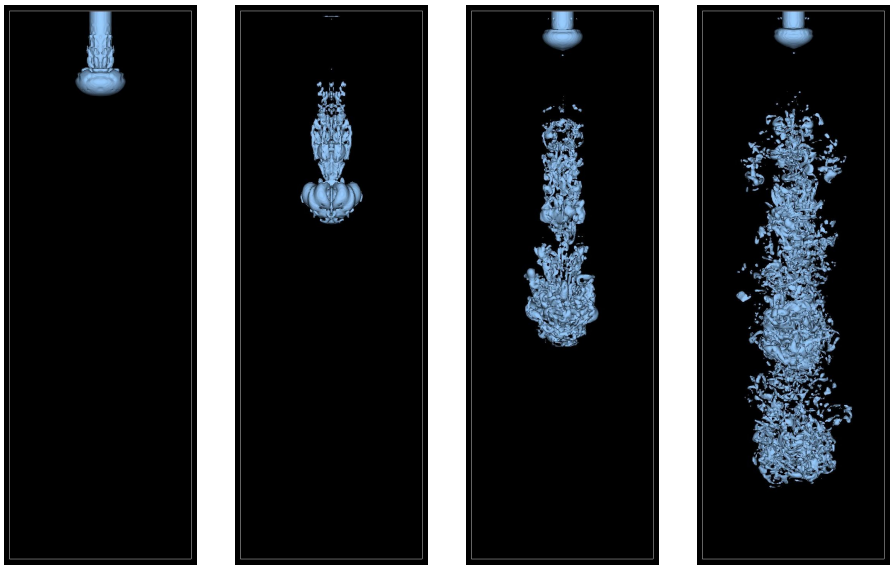

(a) t = 7 (b) t = 19 (c) t = 32 (d) t = 62

Figure 8.13: Pulsed liquid injection, case vof.bI, blue colour represents the liquid phase.

disintegrates at the head just like a continuous injected jet, but also at the tail. Therefore, the pulsed jet breaks up faster into droplets and mixes faster than a continuous jet. Fig. 8.13(c) shows that the first pulse is already completely broken up when the second pulse starts to enter the domain. In Fig. 8.13(d) the third pulse enters the domain.

Fig. 8.14 shows the propagation of the jet of case vof.cII. This case is oriented on Diesel conditions, hence surface tension effects and the liquid density are taken into account. Compared to case vof.bI, one can observe the faster jet propagation due to the larger liquid inertia. The larger surface tension stabilises the pulse and it therefore disintegrates less compared to case vof.bI. The pulse breaks up at its head in the same way as a continuous jet. A large ligament can be observed at the tail that separates from the jet, see Fig. 8.14(d).

In order to monitor the centreline velocity two points are introduced in the domain, similar to experimental settings [41, 42]. As discussed in

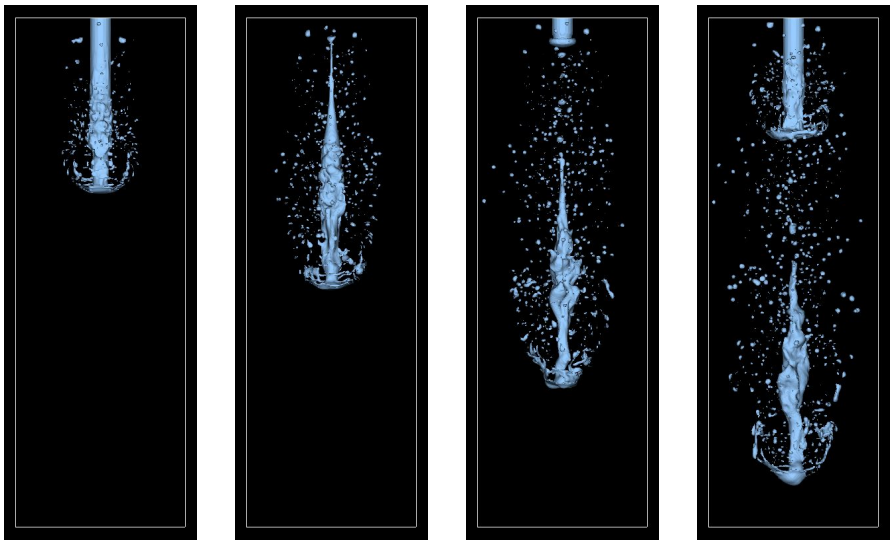

(a) t = 10 (b) t = 16 (c) t = 22 (d) t = 28

Figure 8.14: Pulsed liquid injection, case vof.cII, blue color represents the liquid phase.

Ch. 2.3.6, it has been reported in experimental results, two-dimensional numerical simulations and in simplified analytical models that the tail of the jet moves faster than the head. A ratio of two has been observed between the timespan the head of a pulse needs to travel from point 1 to point 2 and the timespan the tail needs for the same distance. This means that the tail propagates faster than the head. The corresponding results for two VOF and two LPT cases are shown in Fig. 8.15. The simulation results show that the factor 2 is true or very close for some cases, while it equals 1.4 for case vof.b1.

The enhanced gas-liquid mixing for pulsed jets shows to stem from several mechanisms: enhanced air entrainment, a pulse disintegrates when it collides with ligaments stemming from a preceding pulse and additional break-ups at the tail of the pulse. Thus, if one wishes an exact prediction of gas-liquid mixing in pulsed jets, one needs to perform three-dimensional simulations.

To quantify the achieved mixing, the rms of the liquid volume frac-

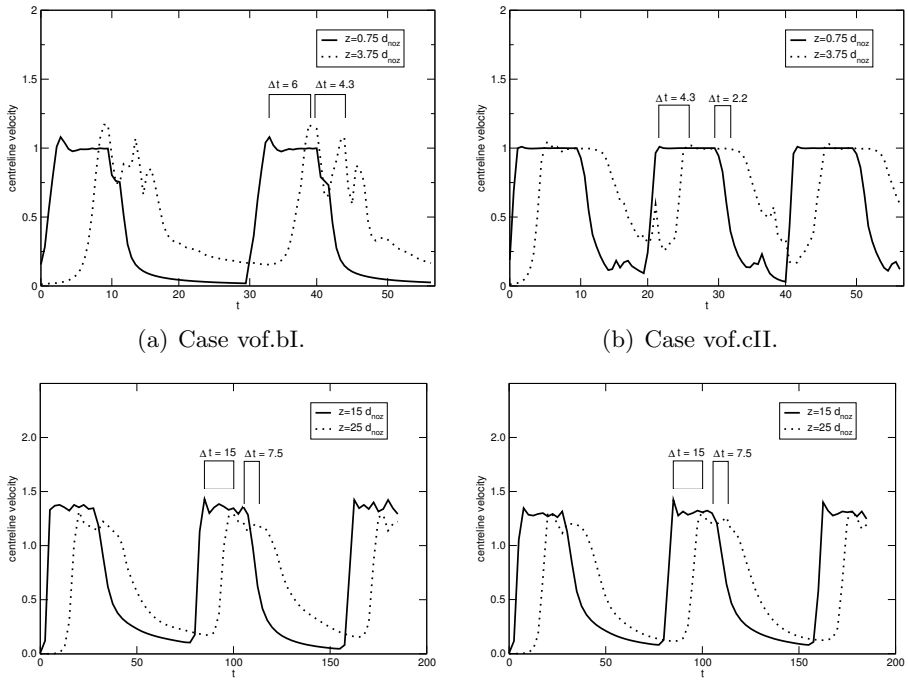

(a) Case vof.bI.

(b) Case vof.cII.

(c) Case lpt.bI.

(d) Case lpt.bII.

Figure 8.15: Center-line axial velocity of the jet vs. time, VOF and LPT cases.

tion in the domain is monitored. This value is normalised to the worst possible rms related to the amount of liquid that is currently present in the domain. This worst possible rms corresponds to a theoretical case where no mixing occurs, thus all liquid is located in a certain amount of cells, while in the other cells no liquid is present. Thus, if the normalised value becomes 1 it relates to no mixing at all, while a value 0 relates to a perfect mixing in the domain. The evolution of this mixing indicator is shown in Fig. 8.16 for the cases vof.cII, vof.dII and vof.eII. The mixing directly after the beginning of the injection is low, but the negative gradient of the curve indicates the improvement of the mixing stemming from the break-up of liquid structures in the domain. The positive gradients at later stages correspond again to injection of liquid mass, which will

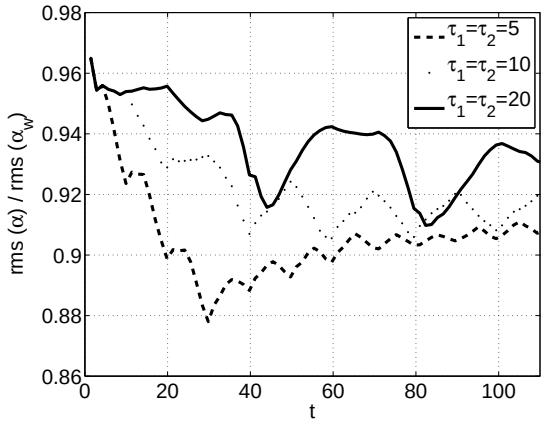

Figure 8.16: Mixing indicator for cases vof.cII, vof.dII and vof.eII.

later mix. Due to this mixing the indicator decreases again during the timespans when no liquid is injected. It can be seen that the mixing, at least for the first few injection pulses, improves with a higher injection frequency.

8.5 Correlation with Experimental Data

The results of the experimental validation are partly published and attached as paper VI. They are summarised in this section and additional results, not yet published, are given.

The strengths of numerical methods as described in the previous chapters are that very detailed data can be extracted and boundary conditions can be changed relatively fast. Commonly one validates numerical methods by comparing with experiments for benchmark flow conditions. But sprays are difficult to visualise as they are optically dense, which is especially problematic for validation purposes, as high accuracy is needed. Thus, experiments usually analyse the global structure of the flow, such as spray penetration length or spray opening angle, and the validation of numerical methods has so far been limited to those [19,101].

This validation of a spray simulation based on only some global parameters involves several drawbacks: First, a LPT simulation contains a large number of model parameters which have intentionally been defined to create a spray that meets the global parameters that are known from experiments. Thus, it should be no surprise, at least for standard flow situations, that e.g. the simulated spray penetration length fits well to experiments. Second, even if two sprays show the same global parameters, their spray structure can be very different from each other. For example the vapour penetration length of a spray is mainly momentum driven. Therefore two sprays can show the same vapour penetration length even if their spatial droplet diameter distributions are very different from each other. Even a one phase jet shows a vapour penetration with a good agreement to a two-phase jet (see [102]), hence, a one parameter correlation cannot be enough for validating the numerical method. Third, until recently experimental and numerical methods have shown inconsistencies in their exact definition of those global parameters.

To overcome these drawbacks, a novel method to correlate experimental and numerical spray data is proposed, based on the light extinction coefficient, μ_e. The approach presented here utilises the capability of the SLIPI technology [103] to suppress multiply scattered light. It has recently been demonstrated that SLIPI-based techniques are able to provide either two or three-dimensional quantitative results of the extinction coefficient even in challenging situations. A further development is Dual-SLIPI [104], where the extinction coefficient field can be extracted directly in two dimensions. It can also be extracted in three dimensions using SLIPI-Scan [105] or Tomo-SLITI [106], but here only a 2-D field is considered.

The main advantage of this approach is that a complete field of a variable, i.e. the extinction coefficient, can be accurately compared. This gives the possibility to assess the numerical modelling of the complete spray structure. Starting from this validation approach, the numerical model can, thereby, be used to extract further detailed information about the spray, such as the droplet diameter distributions, liquid volume fractions, droplet number densities, etc.

Numerical Methods

A LES is performed by applying the LPT approach. The governing equations and numerical methods are the ones described in Ch. 5 and 6.

The intensity of light integrated over all wavelengths, I, is defined as the radiative energy E_r, divided by the angle $d\varphi$ between light beam and the area dA, the area dA, the time interval dt and the solid angle $d\varpi$ [107]:

$$I = \frac{dE_r}{\cos\varphi \cdot dA \cdot dt \cdot d\varpi} \tag{8.2}$$

The extinction coefficient is linked to the light intensity as given by the Beer-Lambert law [108]:

$$dI = -\mu_e \cdot I \cdot dx \tag{8.3}$$

When a beam of light propagates through turbid media over a distance dx, its intensity is attenuated by dI. If the turbid media is a spray, μ_e is only depending on the droplet concentration and their size. If a monodisperse spray is illuminated at a single wavelength, μ_e can be estimated as

$$\mu_e \;=\; \sigma_e \cdot N \;, \tag{8.4}$$

where N is the droplet number density and σ_e the extinction cross-section. The extinction cross-section relates to the effective area of interaction between the incident light beam and the droplets. It is equal to the sum of the scattering and the absorption cross-section. If the droplets are non-absorbing at a certain wavelength, then, only scattering occurs and the scattering-cross section equals the extinction cross-section. The value of the extinction cross-section depends on the droplet diameter, the incident wavelength and the refractive index of the liquid and the surrounding gas. If the droplets are assumed to be spherical, σ_e can be calculated from the Lorenz-Mie theory [109]. This is justified as the study is performed in the dilute spray regime where the droplets are small and surface tension forces, which tend to give the droplets a spherical shape, are dominant. It is also consistent with the assumptions taken for the LPT method. The exact refractive index is unknown a priori and due

to temperature dependency it is varying from droplet to droplet in the spray. A sensitivity study for three refractive indices for the incident wavelength $\lambda = 355\,nm$ in the range of the expected values is performed for droplet diameters between 0 and 40 μm, which are assumed to be relevant in the current application. The selected refractive indices are: one for a non-absorbing fuel of $\varrho = 1.40 - 0.0i$, one for an absorbing fuel of $\varrho = 1.40 - 0.1i$, and one for a non-absorbing fuel of $\varrho = 1.45 - 0.0i$. The differences between the resulting cross-sections are judged to be neglectable. Thus, the refractive index $1.40 + 0.0i$, which corresponds to zero absorption, is used here. By applying these data, the extinction coefficient can be deduced using the droplet distribution function as

$$\mu_e \;=\; \frac{1}{V_c} \int_{V_c} \sum_{1}^{n_p} \sigma_e(d_d) \cdot f dV_c \;, \tag{8.5}$$

where V_c is the size of the analysed volume and n_p is the number of parcels contained in this volume. The volume V_c is given as $V_c = \delta x \cdot \delta y \cdot \Delta z$, which has been chosen according to the volume measured in the experiments: δx and δy correspond to the resolution of the used CCD camera (here 30 μm) and Δz corresponds to the distance between the two laser sheets (2 mm), see the next section for details.

Simulation Set-up

The computational domain is cubical with an edge length of $0.1\,m$. Grid refinements are used, the finest grid which is located where the spray develops has a cell size of $1.5 \cdot 10^{-4}\,m$ in all three directions, which leads to $2.2 \cdot 10^6$ grid cells. Corresponding to the experiment, n-decane is injected through a nozzle of the diameter $d_{noz} = 105\,\mu m$. The liquid velocity at the injection is estimated to $130\,m/s$, the liquid mass flow to $0.5 \cdot 10^{-3} kg/s$. The diameter of the droplets at the injection, are assumed to follow a Rosin-Rammler distribution and a SMD of 10 μm. A sensitivity study for different mass flow rates is performed, as shown later.

Experimental Methods

The validation technique presented here utilises the benefits of two recently developed experimental methods, SLIPI and Dual SLIPI.

When applied to dense transient sprays, laser sheet imaging techniques suffer from multiple scattering issues. Since 2008, a laser sheet imaging based approach called SLIPI [103] has revealed efficient capabilities to suppress light signals resulting from multiple scattered photons (see [110] for details). The principal idea of SLIPI is to use a modulated laser sheet with a sinusoidal incident intensity pattern. While the single light scattering does keep the modulation from the incident pattern, the intensity from the multiple light scattering looses the modulated information.

The amplitude of the modulated component of the detected scattered light can be used to reconstruct the intensity of the single light scattering. a images are recorded, where the modulation is shifted vertically $2\pi/a$ of the spatial period between each of these images. From those a images the complete SLIPI image, S, can be reconstructed, as long as $a \geq 3$, according to

$$S = \frac{\sqrt{2}}{a} \cdot \sqrt{\sum_{i=1}^{a-1} \sum_{j=i+1}^{a} (I_i - I_j)^2} , \tag{8.6}$$

where I are the intensity values from a single recording and the subscripts j and k denote different images.

In 2011, a technique called Dual-SLIPI was developed [104] to further correct issues related to laser extinction and signal attenuation. The extinction coefficient can be obtained quantitatively in two-dimension within the spray region by this technique. In the first step of Dual-SLIPI, two SLIPI images are recorded by simultaneously imaging the laser sheet from both sides with two cameras. In the second step the laser sheet is displaced by a distance Δz within the spray and two more SLIPI images are extracted. Thus, four SLIPI images, $S_{P1,C1}$, $S_{P1,C2}$, $S_{P2,C1}$ and $S_{P2,C2}$ are created. P_1 and P_2 correspond to the two positions of the laser sheets, C_1 and C_2 correspond to the two cameras. The extinction coefficient can be directly determined from these four images,

$$\mu_e \;=\; \ln\left(\frac{S_{P1,C1}\cdot S_{P2,C2}}{S_{P2,C1}\cdot S_{P1,C2}}\cdot\right)\cdot\frac{1}{2\Delta z}\;, \tag{8.7}$$

where Δz is the distance between the two laser sheets. By using Dual-SLIPI, the extinction coefficient can be rapidly measured in two-dimension at the center of the probed spray without the need of advanced reconstruction algorithms.

Experimental Set-up

The experiment referred here has been conducted earlier, a detailed description of the set-up can be found in [111]. The liquid, n-decane, is injected through a nozzle of the diameter $d_{noz} = 105\,\mu m$. The pressure in the vessel is 18.6 bar, the rail pressure is 1100 bar. The temperature of the gas in the vessel is ambient, ca. 20 $°C$. The liquid is injected during a period of 1500 μs. The distance between the two laser sheets is 2 mm. The SLIPI images are taken with two intensified CCD cameras with $1280 \cdot 1024$ pixels and an image pixel resolution of $30\,\mu m \cdot 30\,\mu m$.

Results

The results for the extinction coefficient field are shown in Fig. 8.17. The first three plots on the left show the extinction coefficient field obtained numerically for the time instances $t = 1000, 1500$ and $2000\,\mu s$. The plot to the right shows the extinction coefficient field obtained experimentally by Dual-SLIPI for the time instance $t = 2000\,\mu s$. The injection of the liquid starts at $t = 0$. The plots are cuts through the spray including the injection nozzle, which is located at the bottom of the figure.

When comparing the simulated to the experimental results, the most obvious discrepancy is the capturing of the closing of the nozzle. The experimental results show that the spray is for the time instance after the closure of the nozzle, $t = 2000\,\mu s$, still attached to the nozzle. An apparent explanation is that the nozzle in the experiment does not close completely at 1500 μs, but it starts closing. Thus, there is still liquid injected for some time, even if it is only a small amount compared to injected liquid during the full opening of the nozzle. On the contrary, the nozzle closes sharply at 1500 μs in the numerical simulation, thus,

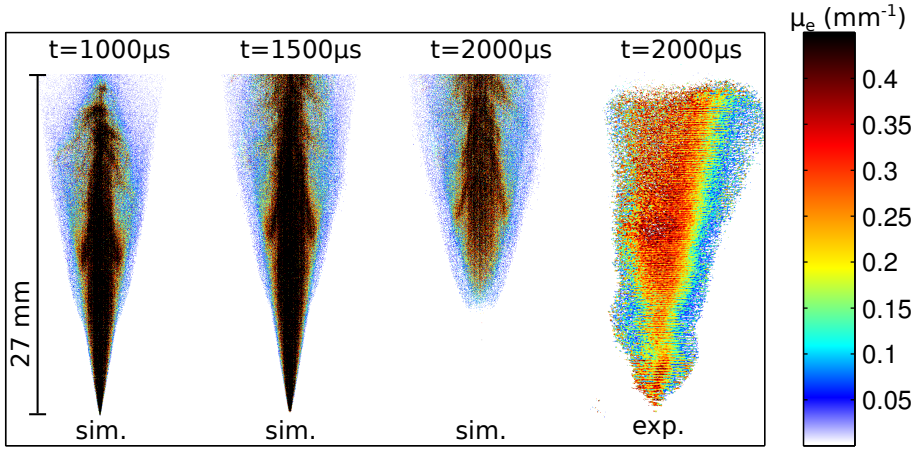

Figure 8.17: Extinction coefficient fields numerically simulated for $t = 1000, 1500$ and $2000\ \mu s$ and measured experimentally for $t = 2000\ \mu s$ (from left to right). The colorbar represents the extinction coefficient field in the units $1/mm$.

the extinction coefficient fields has moved already approximately $10\,mm$ downstream at $t = 2000\ \mu s$ and the spray is not attached to the nozzle anymore.

At $t = 2000\ \mu s$ the numerical results are comparable to the downstream part of the experimentally measured spray which is not yet influenced by the closing of the nozzle. In this region the simulated and measured extinction coefficients are of the same order. Also the spreading of the spray is captured. It shall be noted that the experimental field represents the ensemble average over a 100 single-shots for each modulated image, while the numerical field shows the ensemble average over 5 simulations. Thus, it cannot be expected to find identical values.

When analysing the results, one has to keep in mind that the extinction coefficient field is not a representation of a unique spray, but it represents a certain combination of a droplet number density and related droplet diameters. Thus the same extinction coefficient field can be obtained from e.g. a spray consisting of many small droplets and of

a spray consisting of less larger droplets. Nevertheless, the comparison of the experimental and numerical obtained extinction coefficient fields as shown above give a strong hint that the simulation reflects the spray structure that can be seen in experiments. At least the evidence is a lot stronger as if only a global parameter, e.g. the liquid penetration, is compared.

The presented numerical results suffer in general from the assumptions that are taken when performing a LPT simulation (see Ch. 5). To define more accurate boundary conditions a VOF-LPT coupled approach can be performed, as described in Ch. 7. In the current work a pure LPT approach has been chosen, as the errors stemming from the sources described above are assumed to be significantly larger than the errors stemming from the LPT assumptions.

8.6 Correlation with OpenFOAM

The in-house VOF code is validated through a comparison with the OpenFOAM solver 'interFoam' [112]. The results of this comparison are shown in [113] and summarised in this section[1].

In-house VOF code

The in-house code applies the governing equations and numerical methods as described in Ch. 4. In addition to the discretization schemes given in Ch. 6.1.1, simulations with low-order discretization schemes were performed. These apply a first-order discretization scheme for the convective terms, second-order schemes for the pressure and diffusive terms and first-order schemes for the time derivatives.

OpenFOAM

For comparison the solver 'interFoam' of the open source software package OpenFOAM has been used. The solver uses identical governing equations as the in-house code . In contrast, the equations are discretized by

[1]The OpenFOAM simulations were carried out by A. Vallier, Division of Fluid Mechanics, Lund University.

applying the Finite Volume Method (FVM). As for the in-house code, two sets of discretization orders are applied. The low-order discretizations apply for all terms first-order schemes, while the high-order discretizations apply for all terms second-order schemes. Thus, in terms of discretization order, the in-house low-order discretizations are somewhere in between the OpenFOAM high and low-order discretisations. The in-house high-order discretizations apply significantly higher order discretizations than the OpenFOAM high-order discretizations.

Figure 8.18: Isosurface of the liquid volume fraction at $t = 14.2$ for the high-order cases. Left: OpenFOAM, Right: in-house code. Top: 10 cells/d_{noz}; middle: 20 cells/d_{noz}; bottom: 40 cells/d_{noz}.

Simulation Set-up

The dimensions of the domain and the arrangement of the boundaries are identical to the ones shown in Fig. 8.1. The applied boundary conditions

are as well identical as described in Ch. 8.1. The characteristics of the run case are identical to case C in Tab. 8.1. With both codes several simulations, analysing the effect of different discretization orders and grid resolutions, are performed, see Tab. 8.6.

Code	discretization	grid resolution ($cells/d_{noz}$)
OpenFOAM	low-order	20
OpenFOAM	high-order	20
OpenFOAM	high-order	10
OpenFOAM	high-order	40
in-house	low-order	20
in-house	high-order	20
in-house	high-order	10

Table 8.6: Summary of the set-ups used for comparison of the in-house solver with OpenFOAM.

Results

Snapshots of the development of the liquid jet are shown for the time instance $t = 14.2$ in Fig. 8.18 for the high-order cases given in Tab. 8.6. One can observe that the in-house code produces for the same grid resolution a large amount of small droplets, while OpenFOAM produces a more stable jet.

The liquid penetration length over time is shown for all cases in Fig. 8.19. When comparing the curves of the high-order cases one can observe the same as in the previous figure: while the jet of the in-house cases breaks up and the penetration lengths reaches at some point in time a maximum value of approximately $24\,d_{noz}$, the OpenFOAM jet penetrates nearly linearly with time and no finite penetration can be seen in the domain. Note that the OpenFOAM high-order case with $40\,cells/d_{noz}$ was not run long enough to state that no break up occurs, but it occurs at least significantly later that compared to the in-house code. Interesting is that the low-order case of the in-house code shows a similar behaviour than the OpenFOAM cases: a linear relation between the liquid pene-

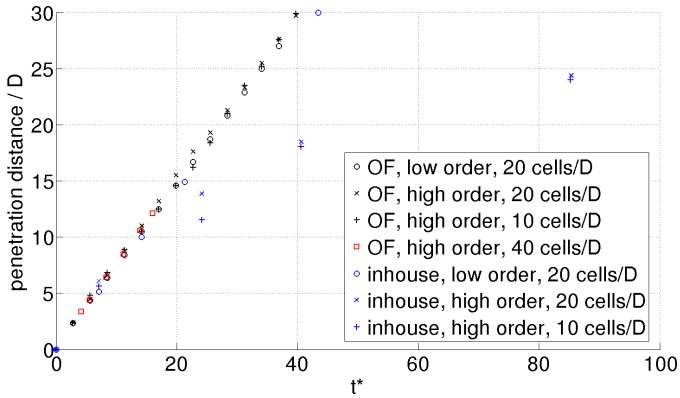

Figure 8.19: Liquid penetration length over time for all cases of Tab. 8.6.

tration length and the injection time. For both cases the jet does not breakup in the domain. Reason is that first or second order discretizations have a high truncation error compared to the high-order case of the in-house code. The truncation order acts as numerical dissipation. This numerical dissipation dissipates turbulent kinetic energy and damps therefore the instabilities that cause the breakup of the jet.

The truncation error goes to zero if the cell size and time-step tend to zero. Thus, the discretization schemes used by the in-house code show the ability to capture the instabilities that cause the jet breakup, while, if OpenFOAM is used, the cell size and timestep have to be chosen significantly smaller.

CHAPTER 9

CONCLUSIONS AND FUTURE WORK

This work is aimed to improve a) the understanding of the underlying physics of atomization and sprays and b) the numerical modelling of such flows.

The influence of varying physical properties of the involved fluids on the breakup of a liquid jet, the development of a spray and its mixing with the surrounding gas has been studied numerically. The stabilising effect of viscosity and surface tension and the destabilising effect of density has been shown for the range of the physical properties under investigation.

The impact of intermittent liquid injection on the breakup characteristics of a liquid jet and the development of a spray has been studied. It has been shown that the tail of an injection pulse propagates faster than its head. This indicates the formation of an entrainment wave that is faster than the jet itself. Pulsed injection has been shown to enhance the jet breakup and liquid-gas mixing.

A novel approach has been developed to couple a VOF simulation of the jet breakup with a LPT simulation of the spray development. Instead of transferring each droplet individually from the VOF to the LPT domain, this approach is based on the idea of only transfer statistical droplet distributions. For a simulated case this has shown to be four times less computational expensive than the direct approach. This

coupling approach can be seen as one step towards the aim to be able to simulate efficient and consistent atomizing two-phase flows, from the in-nozzle flow until evaporation and mixing with ambient gas.

A novel approach has been proposed to correlate experimental with numerical spray data. Instead of correlating only global parameters of the spray, such as liquid penetration length or spray opening angle, here, a complete field of a variable, the light extinction coefficient, has been compared. Experimentally the extinction coefficient is measured by applying the Dual-SLIPI technique. Numerically it was derived from results obtained from the LPT method.

The following issues are proposed to be addressed in future work in order to improve the modelling of the spray:

- The **experimental verification** developed in this thesis can be used to verify a complete spray simulation, from the nozzle to evaporation of the spray, applying the SCA. By that, uncertainties inherent in the LPT method will be removed.
- The mechanisms controlling the flow of **intermittent injection** cases shall be analysed in terms of break-up and liquid-gas mixing.
- The criterion for defining the **position of the statistical CL** can be improved: in addition to using the liquid volume fraction, also the shape of the liquid structures and the spacing between should be taken into account.
- From the topology of the breakup of a liquid jet it is often obvious that the **shape of the statistical CL** should not be planar, but curved.
- To be able to predict a complete fuel spray, the **in-nozzle flow** should be included in the simulation, to take into account the turbulence produced in the nozzle and cavitation effects.

CHAPTER 10

SUMMARY OF THE PUBLICATIONS

Paper I

Holger Grosshans, Robert-Zoltán Szász and Laszlo Fuchs, **Sensitivity Analysis of Spray Dispersion and Mixing for Varying Fuel Properties**, 7^{th} *International Conference on Multiphase Flow, ICMF 2010, Tampa, FL, May 30 – June 4, 2010*

A fuel spray in a combustor has been simulated using the LPT method. Monitoring points have been introduced in the the domain to analyse the spray structure depending on the fuel properties such as fuel surface tension, fuel viscosity and fuel density. The evolution of the spray showed a high sensitivity to variations of fuel properties. Lower surface tension, viscosity and higher fuel density destabilise the droplets and lead to faster breakup. Faster breakup creates smaller droplets, which are stronger affected by turbulent dispersion, evaporate faster and hence mix better with the ambient gas.

The code was developed in previous works by the Division of Fluid Mechanics and extended by the candidate. The candidate carried out new simulations for varying fuel properties, analysed the results and wrote the paper under supervision of Robert-Zoltán Szász and Laszlo Fuchs.

Paper II

Holger Grosshans, Robert-Zoltán Szász and Laszlo Fuchs, **Numerical Simulation of the Primary Breakup of a Liquid Fuel Jet**, *Int. Conf. on Jets, Wakes and Separated Flows, ICJWSF-2010, September 27-30, 2010, Cincinnati, Ohio, USA*

Two liquid jets of the Weber numbers 10000 and 100000 have been simulated using the VOF method. It has been shown how aerodynamic instabilities lead to the disintegration of the intact liquid core, which forms ligaments and droplets. A coupling layer has been developed to identify liquid droplets, their radius, position and velocity. Several test cases were run, which show that the algorithm of this layer delivers accurate results if a droplet is resolved by at least three grid cells. This coupling layer was introduced close to the outlet of the domain. The results showed that the droplet of the case of the smaller Weber number are in average larger and travel faster downstream than the droplets of the case of the higher Weber number.

The code was developed in previous works by the Division of Fluid Mechanics and extended by the candidate. The candidate developed the algorithm of the coupling layer, carried out the simulations, analysed the results and wrote the paper under supervision of Robert-Zoltán Szász and Laszlo Fuchs.

Paper III

Holger Grosshans, Robert-Zoltán Szász and Laszlo Fuchs, **Simulation of the Primary Breakup of a Liquid Fuel Jet to Create Starting Conditions for a LPT Spray Simulation**, *AIAA 2011-770, 49th AIAA Aerospace Sciences Meeting including the New Horizons Forum and Aerospace Exposition, 4 - 7 January 2011, Orlando, Florida*

Three liquid jets with different Weber numbers and gas-liquid density ratios are simulated. A coupling layer has been introduced close to the outlet of the domain to extract time dependent and time averaged data of the liquid and gaseous phase. The aim of the work is to create datasets that can be used as starting condition for spray simulations using the LPT method. The position of the coupling layer has been defined

depending on the local liquid volume fraction.

The code was developed in previous works by the Division of Fluid Mechanics and extended by the candidate. The candidate carried out the simulations, analysed the results and wrote the paper under supervision of Robert-Zoltán Szász and Laszlo Fuchs.

Paper IV

Holger Grosshans, Robert-Zoltán Szász and Laszlo Fuchs, **Development of a combined VOF-LPT method to simulate two-phase flows in various regimes**, *7th International Symposium on Turbulence and Shear Flow Phenomena (TSFP-9), 28 - 31 July 2011, Ottawa, Canada*

The previously developed SCA is applied to simulate a Diesel like case. A LES for the full spray from injection to evaporation is performed.

The code was developed in previous works by the Division of Fluid Mechanics and extended by the candidate. The candidate developed the VOF-LPT coupling algorithm, carried out the simulations, analysed the results and wrote the paper under supervision of Robert-Zoltán Szász and Laszlo Fuchs.

Paper V

Holger Grosshans, Robert-Zoltán Szász and Laszlo Fuchs, **Full Spray Simulation - Coupled Volume of Fluid and Lagrangian Particle Tracking methods**, *24th European Conference on Liquid Atomization and Spray Systems (ILASS-24), 5 - 7 September 2011, Estoril, Portugal*

In this work the SCA is developed. Liquid structures are identified at a defined plane in the VOF domain and datasets of their properties are created. These datasets are used to derive statistical distributions. A procedure based on the Monte-Carlo method is developed to inject droplet parcels in the LPT simulation by using these statistical droplet property distributions. The significant increase of computational efficiency compared to other coupling approaches has been demonstrated.

The code was developed in previous works by the Division of Fluid

Mechanics and extended by the candidate. The candidate developed the algorithm of extracting the droplets in the VOF domain and the algorithm of injecting droplets in the LPT domain, carried out the simulations, analysed the results and wrote the paper under supervision of Robert-Zoltán Szász and Laszlo Fuchs.

Paper VI

Holger Grosshans, Eduard Berrocal, Elias Kristensson, Robert-Zoltán Szász and Laszlo Fuchs, **Correlating Results from Numerical Simulation to SLIPI-based Measurements for a non-combusting Diesel Spray**, *12th International Conference on Liquid Atomization and Spray Systems (ICLASS-12), 2 - 6 September 2012, Heidelberg, Germany*

A novel method is proposed to correlate experimental and numerical spray results, based on the extinction coefficient. Experimentally the extinction coefficient field can be obtained by applying the Dual-SLIPI technology. In this work the algorithm to derive the extinction coefficient field from the results of a LPT simulation is developed. Main advantage of this approach is that not only global spray parameters like penetration distance or spray opening angle are compared but a complete field of a variable.

The code was developed in previous works by the Division of Fluid Mechanics and extended by the candidate. The candidate developed the method to derive the local extinction coefficient numerically, carried out the simulations, analysed the results and wrote the paper under supervision of Eduard Berrocal, Robert-Zoltán Szász and Laszlo Fuchs. The experiments where carried out by the Division of Combustion Physics, Lund University.

Paper VII

Holger Grosshans, Alexander Nygård and Laszlo Fuchs, **Mixing Due Pulsating Turbulent Jets**, *to appear in Progress in Turbulence V, Proceedings of the iTi Conference in Turbulence 2012, Springer Proceedings in Physics, Springer*

It has been observed that a pulsating jet creates at the tail of the injection pulse an entrainment wave which travels faster than the pulse itself. This entrainment wave enhances the air entrainment and therefore the mixing. Previous works on this topic were either experiments, simplified CFD simulations or very simplified analytical models. In this work full VOF simulations are performed to study this effect. The characteristics of the injection pulses are varied to study the influence on the mixing process.

The code was developed in previous works by the Division of Fluid Mechanics and extended by the candidate. The candidate carried out the simulations, analysed the results and supported to write the paper.

Paper VIII

Holger Grosshans, Alexander Nygård and Laszlo Fuchs, **Fuel jet mixing enhanced by intermittent injection**, *51st AIAA Aerospace Sciences Meeting Including the New Horizons Forum and Aerospace Exposition, 7 - 10 January 2013, Grapevine (Dallas/Ft. Worth Region), Texas*

The effect of intermittent injection on the mixing of a fuel spray with the surrounding air is studied. Theoretical considerations show the direct dependence of the formation of vortices on density gradients in the flow. The performed VOF and LPT simulations show that depending on the physical properties of the liquid and the gas, turbulent mixing can be enhanced significantly.

The code was developed in previous works by the Division of Fluid Mechanics and extended by the candidate. The candidate carried out the simulations, analysed the results and supported to write the paper.

Paper IX

Holger Grosshans, Robert-Zoltán Szász and Laszlo Fuchs, **Simulation of the Breakup of a Liquid Fuel Jet**, *Manuscript, submitted to Atomization and Sprays, January 2013*

The primary breakup of a liquid jet is simulated using the VOF method. A coupling layer is introduced at which statistical data about

the droplet size distribution, radial location as well as mean and fluctuating velocity are extracted The code and the set-up are verified concerning the size of the domain, the cell size, the location of the coupling layer and the accuracy of the implementation. The location of the coupling layer is determined depending on a liquid volume fraction criterion. The main contribution of this paper is the establishment of the above mentioned statistical method and the generation of initial conditions for the dilute spray modelling, using LPT.

The code was developed in previous works by the Division of Fluid Mechanics and extended by the candidate. The candidate carried out the simulations, analysed the results wrote the paper under supervision of Robert-Zoltán Szász and Laszlo Fuchs.

Paper X

Holger Grosshans, Robert-Zoltán Szász and Laszlo Fuchs, **Development of an Efficient Statistical VOF-LPT Coupling Method**, *Manuscript, submitted to International Journal for Numerical Methods in Fluids, February 2013*

The SCA is developed to couple a VOF with a LPT simulation. An exemplary case is simulated using the SCA and the DCA and the results of both simulations are compared. It is shown that the SCA is accurate and computationally significantly more efficient than the DCA.

The code was developed in previous works by the Division of Fluid Mechanics and extended by the candidate. The candidate developed the VOF-LPT coupling algorithm, carried out the simulations, analysed the results and wrote the paper under supervision of Robert-Zoltán Szász and Laszlo Fuchs.

ACKNOWLEDGEMENTS

The computations were run at the center for scientific and technical computing for research at Lund University, LUNARC. The work was financed by the Swedish Foundation for Strategic Research (SSF), the Swedish Energy Authority (STEM) and the Center for Combustion Science and Technology (CeCOST).

I would like to thank my supervisor Prof. Laszlo Fuchs and my co-supervisor Dr. Robert-Zoltán Szász for giving me the opportunity to work in an exciting environment, which I enjoyed every day, and for their excellent support in the past four years.

I want to thank Dr. Eduard Berrocal and Dr. Christophe Duwig for their creative and inspiring ideas, I hope we will keep on collaborating. Thanks to Prof. Xue-Song Bai, Dr. Mehdi Jangi and Dr. Rixin Yu for the discussions and creating a nice working atmosphere. A special thanks to Prof. Johan Revstedt for spending one of his Sundays in the summer of 2008 to show me the university and to convince me to come to Lund, which I never regretted. I also want to thank Dr. Mireia Altimira and Alexander Nygård for the very friendly cooperation.

I am grateful that I met many PhD students I made friends with in the division: Eric, Piero, Erdzan for proof reading my thesis, Jiangfei, Fan. Tobias for preventing me from burning down Fysikum. Alper, Henning, Hessam and Rickard for sharing Ariman beers. It was a pleasure for me to spend my time with everybody in the Division of Fluid Mechanics. I

had a great time filling our cupboard with NaN trophies of all the sports competitions we were zlatanizing!

Finally, I want to thank my parents for their constant support and for bearing that I am far away from Hockenheim for such a long time already.

BIBLIOGRAPHY

[1] A. Farth, C. Fettes, and A. Leipertz. Investigation of the Diesel Spray Break-Up Close to the nozzle at different Injection conditions. *The Fourth International Symposium COMODIA 98*, 1998.

[2] A.H. Lefebvre. The Role of Fuel Preperation in Low-Emission Combustion. *Journal of Engineering for Gas Turbines and Power*, 117:617–654, October 1995.

[3] W.J.G. Bräunling. *Flugzeugtriebwerke*. Springer Verlag Berlin Heidelberg New York, 2001.

[4] G.M. Faeth, L.-P. Hsiang, and P.K. Wu. Structure and breakup properties of Sprays. *Int. J. Multiphase Flow*, 21:99–127, 1995.

[5] Jeffrey D. Naber and Dennis L. Siebers. Effects of Gas Density and Vaporization on Penetration and Dispersion of Diesel Sprays. *SAE International*, 96(0034), February 1996.

[6] S. Martinez-Martinez, F.A. Sanchez-Cruz, J.M. Riesco-Avila, A. Gallegos-Munoz, and S.M. Aceves. Liquid penetration length in direct diesel fuel injection. *Applied Thermal Engineering*, 2007.

[7] Zhijun Wu, Zhiyong Zhu, and Zhen Huang. An experimental study on the spray structure of oxygenated fuel using laser-based visualization and particle image velocimetry. *Fuel*, 85, 2006.

[8] E. Berrocal, E. Kristensson, D. Sedarsky, and M. Linne. Analysis of the SLIPI technique for multiple scattering supression in planar imaging of fuel sprays. *ICLASS 2009*, 2009.

[9] M. Paciaroni, E. Berrocal, D. Sedarsky, and M.A. Linne. Ballistic imaging of liquid breakup processes. *Proc. Combust. Inst.*, 2009.

[10] T. Anderson and R. Jackson. A fluid mechanical description of fluidized beds. *Ind. Eng. Chem. Fundam.*, 6(4):527–539, 1967.

[11] M. Ishii. Thermo-fluid dynamic theory of two-phase flow. *Direction de Etudes et Recherches d'Electricite de France*, 1975.

[12] A. Benavides and B. van Wachem. Eulerian-Eulerian prediction of the dilute turbulent gas-particle flow in a backward-facing step. *International Journal of Heat and Fluid Flow*, 30:452–461, 2009.

[13] Ming Jia, Maozhao Xie, Hong Liu, Wei-Haur Lam, and Tianyou Wang. Numerical simulation of cavitation in the conical-spray nozzle for diesel premixed charge compression ignition engines. *Fuel*, 90(8):2652–2661, 2011.

[14] Weixing Yuan and Günter H. Schnerr. Numerical simulation of two-phase flow in injection nozzles: Interaction of cavitation and external jet formation. *Journal of Fluids Engineering*, 125(6):963–969, 2003.

[15] S. Som, S.K. Aggarwal, E.M. El-Hannouny, and D.E. Longman. Investigation of nozzle flow and cavitation characteristics in a diesel injector. *Journal of Engineering for Gas Turbines and Power*, 132(4):042802, 2010.

[16] A. Vallet, A. A. Burluka, and R. Borghi. Development of a Eulerian Model for the "Atomization" of a Liquid Jet. *Atomization and Sprays*, 11:619–642, 2001.

[17] George A. Siamas, Xi Jiang, and Lutz C. Wrobel. Direct numerical simulation of the near-field dynamics of annular gas-liquid two-phase jets. *Physics of Fluids*, 21(042103):1–14, April 2009.

[18] J. Shinjo and A. Umemura. Simulation of liquid jet primary breakup: Dynamics of ligament and droplet formation. *International Journal of Multiphase Flow*, 36:513–532, 2010.

[19] J.K. Dukowicz. A Particle-Fluid Numerical Model for Liquid Sprays. *Journal of computational Physics*, 1978.

[20] C.S. Lee and S.W. Park. An experimental and numerical study on fuel atomization characteristics of high-pressure diesel injection sprays. *Fuel*, 81, 2002.

[21] Pogorevc P., Kegl B., and Skerget L. Diesel and Biodiesel Fuel Spray Simulations. *Energy & Fuels*, 2008, 2007.

[22] Ville Vuorinen, Martti Larmi, and Laszlo Fuchs. Large-Eddy Simulation of particle size distribution effects on turbulence in sprays. *46th AIAA Aerospace Sciences Meeting and Exhibit,*, 2008.

[23] Ville Vuorinen, H. Hillamo, O. Kaario, M. Larmi, and Laszlo Fuchs. Large Eddy Simulation of Droplet Stokes Number Effects on Turbulent Spray Shape. *Atomization and Sprays*, 20(2):93–114, 2010.

[24] Gaurav Tomar, Daniel Fuster, Stéphane Zaleski, and Stéphane Popinet. Multiscale simulations of primary atomization. *Computers & Fluids*, 39(10):1864–1874, 2010.

[25] Marcus Herrmann. Detailed Numerical Simulations of the Primary Atomization of a Turbulent Liquid Jet in Crossflow. *ASME Turbo Expo 2009: Power for Land, Sea and Air, GT2009*, June 2009.

[26] D. C. Leslie and G. L. Quarini. The application of turbulence theory to the formulation of subgrid modelling procedures. *Journal of Fluid Mechanics*, 91:65–91, 1979.

[27] S.B. Pope. *Turbulent Flows*. Cambridge University Press, 2000.

[28] Sir G.I. Taylor. Statistical Theory of Turbulence. *Proceedings of the Royal Society of London. Seies A, Mathematical and Physical Sciences*, 151(873):421–444, 1935.

[29] Lord J.W.S. Rayleigh. Investigation of the character of the equilibrium of an incompressible heavy fluid of variable density. *Proceedings of the London Mathematical Society*, 14:170–177, 1883.

[30] Sir G.I. Taylor. The instability of liquid surfaces when accelerated in a direction perpendicular to their planes. *Proceedings of the Royal Society of London. Seies A, Mathematical and Physical Sciences*, 201:192–196, 1950.

[31] Lord W.T. Kelvin. Hydrokinetic solutions and observations. *Philosophical Magazine*, 42(42):362–377, 1871.

[32] H. v. Helmholtz. Ueber discontinuierliche Fluessigkeits-Bewegungen. *Monatsberichte der Königlichen Preussische Akademie der Wissenschaften zu Berlin*, (23):215–228, 1868.

[33] L. Prahl, A. Hölzer, D. Arlov, J. Revstedt, M. Sommerfeld, and L. Fuchs. On the interaction between two fixed spherical particles. *International Journal of Multiphase Flow*, 2007.

[34] S. Elgobashi. On Predicting Particle-Laden Turbulent Flows. *Applied Scientific Research*, 52:309–329, 1994.

[35] R.D. Reitz. Computer Modeling of Sprays. Spray Technology Short Course, Pittsburgh, PA, 1994.

[36] C.T. Crowe, J.N. Chung, and T.R. Troutt. Particle Mixing in Free Shear-flows. *Prog. Energy Combust. Sci*, 14:171–194, 1988.

[37] J.D. Kulick, J.R. Fessler, and J.K. Eaton. Particle response and turbulence modification in fully developed channel flow. *Journal of Fluid Mechanics*, 277:109–34, October 1994.

[38] J.K. Eaton. Two-way coupled turbulence simulations of gas-particle flows using point-particle tracking. *International Journal of Multiphase Flow*, 35(9):792–800, September 2009.

[39] S.P. Lin and R.D. Reitz. Drop and Spray Formation from a Liquid Jet. *Annu. Rev. Fluid Mech.*, 30:85–105, 1998.

[40] A. Wierzba. Deformation and breakup of liquid drops in a gas stream at nearly critical Weber numbers. *Experiments in Fluids*, 9:59–64, 1990.

[41] P.O. Witze. The impulsively started incompressible turbulent jet. *Energy Rep.*, SAND80-8617, 1980.

[42] P.O. Witze. Hot-film anemometer measurements in a starting turbulent jet. *AIAA Journal*, 21:308–309, 1983.

[43] M.P.B. Musculus and K. Kattke. Entrainment Waves in Diesel Jets. *SAE*, 01(1355), 2009.

[44] M.P.B. Musculus. Entrainment waves in decelerating transient turbulent jets. *Journal of Fluid Mechanics*, 638:117–140, 2009.

[45] M. Birkinshaw. Instabilities in astrophysical jets. *Astrophysics and Space Science*, 242(1-2):17–91, 1996.

[46] Attilio Ferrari. Modeling Extragalactic Jets. *Annual Review of Astronomy and Astrophysics*, 36(1):539–598, 1998.

[47] Bo Reipurth and John Bally. HERBIG-HARO FLOWS: Probes of Early Stellar Evolution. *Annual Review of Astronomy and Astrophysics*, 39(1):403–455, 2001.

[48] M. Belan, M. Mirzaei, S. De Ponte, and D. Tordella. An experimental setup for visualizations and measurements on free hypersonic jets. *EPJ Web of Conferences*, 25:01056 (14 pp.), 2012.

[49] D. Tordella, M. Belan, S. Massaglia, S. De Ponte, A. Mignone, E. Bodenschatz, and A. Ferrari. Astrophysical jets: insights into long-term hydrodynamics. *New Journal of Physics*, 13(043011), 2011.

[50] Charles L. Feffermann. Existence and Smoothness of the Navier-Stokes Equation. *Princeton University, Departement of Mathematics*, NJ 08544-1000, May 2000.

[51] B.S. Baldwin and H. Lomax. Thin-lzyer approximation and algebraic model for seperated turbulent flow. *AIAA*, 78(257), 1978.

[52] W.P. Jones and B.E. Launder. The prediction of laminarization with a two-equation model of turbulence. *Int. J. Heat Mass Transfer*, 15:301–314, 1972.

[53] E.G. Tulapurkara. Turbulence Models for the Computation of Flow past Airplanes. *Prog. Aerospace Sci.*, 33:71–165, 1997.

[54] M.S. Salim, S.C. Cheah, and A. Chan. Numerical Simulation of dispersion in urban street canyons with avenue-like tree plantings: Comparison between RANS and LES. *Building and Environment*, 46:1735–1746, 2011.

[55] J. Smagorinsky. General circulation experiments with the primitive equations: I. The basic equations. *Mon. Weather Rev.*, 91:99–164, 1963.

[56] M. Germano, U. Piomelli, P. Moin, and W.H. Cabot. A dynamic subgridscale eddy viscosity model. *Physics of Fluids*, pages 1760–1765, 1991.

[57] J. Bardina, H. Ferziger, and W.C. Reynolds. Improved subgrid models for large eddy simulation. *AIAA Paper*, 80(1357), 1980.

[58] S. Liu, C. Meneveau, and J. Katz. On the properties of similarity subgrid-scale models as deduced from measurements in a turbulent jet. *Journal of Fluid Mechanics*, 275:83–119, 1994.

[59] J.P. Boris, F.F. Grinstein, E.S. Oran, and R.L. Kolbe. New insights into large eddy simulation. *Fluid Dyn. Res.*, 100:199–228, 1992.

[60] M. Rudman. A volume-tracking method for incompressible multifluid flows with large density variations. *Int. J. Num. Meth. Fluids*, 28:357–378, 1998.

[61] J.U. Brackbill, D.B. Kothe, and C. Zemach. A continuum method for modeling surface tension. *Journal of Computational Physics*, 100:335–354, 1992.

[62] D. Lörstad. Numerical modeling of deforming bubble transport related to cavitating hydraulic turbines. *Doctoral Thesis*, August 2003.

[63] E.G. Puckett, A.S. Almgren, J.B. Bell, D.L. Marcus, and W.J. Richter. A high-order projection method for tracking fluid interfaces in variable density incompressible flows. *Journal of Computational Physics*, 130:269–282, 1997.

[64] Y. Renardy and M. Renardy. Prost: A parabolic reconstruction of surface tension for the volume of fluid method. *Journal of Computational Physics*, 183:400–421, 2002.

[65] D. Lörstad, M. Francois, W. Shyy, and L. Fuchs. Assessment of volume of fluid and immersed boundary methods for droplet computations. *Int. J. Num. Meth. Fluids*, 46:109–125, 2004.

[66] D. Löstad, M. Francois, W. Shyy, and L. Fuchs. Volume of Fluid ans Immersed Boundary Investigations of a Single Rising Droplet. $AIAA,\ 41^{st} Aerospace Science Meeting and Exibith.$, (1282), 2003.

[67] V.R. Gopala and B. van Wachem. Volume of fluid methods for immiscible-fluid and free surface flows. *Chemical Engineering Journal*, 141:204–221, 2008.

[68] S.O. Unverdi and G. Tryggvarson. A front tracking method for viscous incompressible multi-fluid flows. *Journal of Computational Physics*, 100:25–37, 1992.

[69] S. Osher and J.A. Sethian. Fronts propagating with curvature-dependent speed: algorithms based on Hamilton-Jacobi formulations. *Journal of Computational Physics*, 79:234–246, 1988.

[70] J.A. Sethian. A fast marching level-set method for monotonically advancing fronts. *Proc. Natl. Acad. Sci. USA*, 93:1591–95, 1996.

[71] F.H. Harlow and J.E. Welch. Numerical calculation of time-dependent viscous incompressible flow of fluid with free surface. *Physics of Fluids*, 8(12):2182–2189.

[72] C.W. Hirt and B.D. Nichols. Volume of Fluid (VOF) method for the dynamics of free boundaries. *Journal of Computational Physics*, 39:201–225, 1981.

[73] M. Rudman. Volume-tracking Methods for Interfacial Flow Calculations. *Int. J. Num. Meth. Fluids*, 24:671–691, 1997.

[74] D.L. Young. Time-dependent multi-material flow with large fluid distortion. *Numerical Methods for Fluid Dynamics*, pages 273–285, 1982.

[75] W.F. Noh and P. Woodward. SLIC (simple line interface calculation). *Lecture Notes in Physics*, 59:330–340, 1976.

[76] B. van Wachem and J.C. Schouten. Experimental validation of a 3-d Lagrangian VOF model: Bubble shape and rise velocity. *AIChE*, 48(12):2744–2753, 2002.

[77] O. Ubbink. Numerical Prediction of Two fluid systems with sharp interfaces. *PhD Thesis*, 1997.

[78] H. Jasak and H.G. Weller. Interface-tracking capabilities of the InterGamma differencing scheme. *Technical Report*, 1995.

[79] L. Schiller and A.Z. Neumann. A drag coefficient correlation. *Ver. Deut. Ing.*, 77:318–320, 1993.

[80] M Zastawny, G. Mallouppas, F. Zhao, and B. van Wachem. Derivation of drag and lift force and torque coefficients for non-spherical particles in flows. *International Journal of Multiphase Flow*, 39:227–239, 2012.

[81] M. Sommerfeld, C. Crowe, and Y. Tsuji. *Multiphase Flows with Droplets and Particles*. CRC Press, November 1997.

[82] Mirko Salewski. *LES of Jets and Sprays injected into Crossflow*. PhD thesis, Lund University of Technology, 2006.

[83] D. Caraeni, C. Bergström, and L. Fuchs. Modeling of Liquid Fuel Injection, Evaporation and Mixing in a Gas Turbine Burner Using

Large Eddy Simulation. *Flow, Turbulence and Combustion*, 65(223-244), 2000.

[84] R.D. Reitz and R. Diwakar. Effect of Drop Breakup on Fuel Sprays. *SAE Technical Paper*, 860469, 1986.

[85] C. Bergström. *Numerical Modelling of Fuel Sprays.* PhD thesis, Lund University of Technology, June 1999.

[86] P.J. O'Rourke and A.A. Amsden. The TAB Model for Numerical Calculation of Spray Breakup. *SAE Technical Paper*, 872089, 1978.

[87] A.A. Amsden, P.J. O'Rourke, and T. Butler. KIVA-II: A Computer Program for Chemically Reactive Flows with Sprays. *Los Alamos National Laboratory*, (Tech. Rep. LA-11560-MS), 1989.

[88] W.E. Ranz and W.R. Marshall. Evaporation from drops - I and II. *Chem. Engr. Prog.*, 48(141 and 173), 1952.

[89] Man Mohan Rai and Parviz Moin. Direct Simulations of Turbulent Flow Using Finite-Difference Schemes. *Journal of computational Physics*, 96:15–53, 1991.

[90] G.S. Jang and C.W. Shu. Efficient implementation of weighted ENO schemes. *Journal of computational Physics*, 126:202–228, 1996.

[91] L.S. Caretto, A.D. Gosman, S.V. Patankar, and D.B. Spalding. Two calculation procedures for steady, three-dimensional flows with recirculation. *3rd International Conference on Numerical Methods in Fluid Mechanics. II*, July 1972.

[92] S.V. Patankar. Numerical Prediction of Three-Dimensional Flows. *Studies in Convection: Theory, Measurement and Applications*, 1:1–78, 1975.

[93] J. Gullbrand, X.S. Bai, and L. Fuchs. High-Order Cartesian Grid Method for Calculation of Incompressible Turbulent Flows. *Int. J. Num. Meth. Fluids*, 36:687–709, 2001.

[94] ASME. Procedure for Estimation and Reporting of Uncertainty Due to Discretization in CFD Applications. *J. Fluids Eng*, 130(078001), July 2008.

[95] L.F. Richardson. The approximate arithmetical solution by finite differences of physical problems involving differential eqiations with an application to the stresses in a masonry dam. *Trans. Roy. Soc. London*, Ser. A(210):307–357, 1910.

[96] D.A. Herbert, D.P. Schmidt, D.A. Knaus, S. Philips, and P.J. Magari. Parallel VOF Spray Droplet Identification in an Unstructured Grid. *ILASS Americas, Orlando, Florida, May 2008*, 2008.

[97] Eugene Lubarsky, Jonathan R. Reichel, Ben T. Zinn, and Rob McAmis. Spray in Crossflow: Dependence on Weber Number. *Journal of Engineering for Gas Turbines and Power*, 132(021501):1–9, February 2010.

[98] O. Tammisola, F. Lundell, and L.D. Söderberg. Surface tension-induced global instability of planar jets and wakes. *Journal of Fluid Mechanics*, 713:632–658, 2012.

[99] O. Tammisola, A. Sasaki, F. Lundell, A. Matsubara, and L.D. Söderberg. Stabilizing effect of surrounding gas flow on a plane liquid sheet. *Journal of Fluid Mechanics*, 672:5–32, 2011.

[100] T. Funada, D.D. Joseph, and S. Yamashita. Stability of a liquid jet into incompressible gases and liquids. *Int. J. Multiphase Flow*, 30:1279–1310, 2004.

[101] J.C. Beck and A.P. Watkins. On the Development of Spray Submodels Based on Droplet Size Moments. *Journal of Computational Physics*, 182:586–621, May 2002.

[102] Mirko Salewski, Dragan Stankovic, and Laszlo Fuchs. A comparison between a Single- and Multiphase Jet in Crossflow Using LES. *J. Eng. Gas Turbines and Power*, 129(1), 2007.

[103] E. Berrocal, E. Kristensson, and M. Richter. Application of structured illumination for multiple scattering suppression in planar

laser imaging of dense sprays. *Opt. Express*, 16:17870–17881, October 2008.

[104] E. Kristensson, E. Berrocal, and M. Alden. Extinction coefficient imaging of turbid media using dual structured laser illumination planar imaging. *Opt. Lett.*, 36(9):1656–1658, May 2011.

[105] R Wellander, E. Berrocal, E. Kristensson, M. Richter, and M. Alden. Three-dimensional measurement of the local extinction coefficient in a dense spray. *Meas. Sci. Technol.*, 22, 2011.

[106] E. Kristensson, E. Berrocal, and M. Alden. Quantitative 3D imaging of scattering media using Structured Illumination and Computed Tomography. *submitted to Opt. Express*, 2012.

[107] G. Rybicki and A. Lightman. Radiation Processes in Astrophysics. *John Wiley & Sons*, 1979.

[108] J.H. Lambert. Photometria, sive de mensura et gradibus luminis, colorum et umbrae. *Sumptibus Vidae Eberhardi Klett*, 1760.

[109] C. Bohren and D. Huffman. Absorption and scattering of light by small particles. *Wiley, N.Y.*, 1983.

[110] E. Kristensson. Structured Laser Illumination Planar Imaging, SLIPI, Applications for Spray Diagnostics. *PhD Thesis*, April 2012.

[111] E. Berrocal, E. Kristensson, P. Hottenbach, M. Alden, and G. Gruenefeld. Quantitative imaging of a non-combusting Diesel spray using Structured Laser Illumination Planar Imaging. *Appl. Phys. B, Lasers and Optics*, October 2012.

[112] http://www.openfoam.com/.

[113] Aurélia Vallier, Holger Grosshans, Johan Revstedt, and Laszlo Fuchs. Numerical Simulation of the Breakup of a Liquid Jet using the OpenFoam VOF method and Comparison to an In-house Code. *6th OpenFoam Workshop, PennState University, USA, June 13-16, 2011*, March 2011.